HHS Public Access

Author manuscript

Neuron. Author manuscript; available in PMC 2022 July 21.

Published in final edited form as:

Neuron. 2021 July 21; 109(14): 2256–2274.e9. doi:10.1016/j.neuron.2021.05.023.

Specific and behaviourally consequential astrocyte G_q GPCR signaling attenuation *in vivo* with iβARK

Jun Nagai[1,11], **Arash Bellafard**[2], **Zhe Qu**[9], **Xinzhu Yu**[1,12], **Matthias Ollivier**[1], **Mohitkumar R. Gangwani**[1], **Blanca Diaz-Castro**[1], **Giovanni Coppola**[2,4,5], **Sarah M Schumacher**[10], **Peyman Golshani**[1,2,5,6,7,8], **Viviana Gradinaru**[9], **Baljit S. Khakh**[1,3,13,*]

[1]Department of Physiology

[2]Department of Neurology

[3]Department of Neurobiology

[4]Department of Psychiatry and Biobehavioral Sciences, David Geffen School of Medicine

[5]Center for Neurobehavioral Genetics, Semel Institute for Neuroscience and Human Behavior,

[6]Integrative Center for Learning and Memory, University of California Los Angeles, Los Angeles, CA 90095-1751, USA

[7]West LA Veterans Affairs Medical Center, Los Angeles, CA 90073, USA

[8]Intellectual and Developmental Disabilities Research Center, Los Angeles, CA, USA

[9]Division of Biology and Biological Engineering, California Institute of Technology, Pasadena, CA 91125, USA

[10]Department of Cardiovascular & Metabolic Sciences, Lerner Research Institute, Cleveland Clinic, 9500 Euclid Avenue, Cleveland, Ohio 44195, USA

[11]RIKEN Center for Brain Science, 2-1 Hirosawa Wako City, Saitama 351-0198 JAPAN

[12]Department of Molecular and Integrative Physiology, University of Illinois at Urbana-Champaign, 514 Burrill Hall, 407 S. Goodwin Ave, Urbana, IL 61801

[13]Lead contact

[*]Correspondence bkhakh@mednet.ucla.edu.

Current address BD-C Group Leader, UK Dementia Research Institute and Centre for Discovery Brain Sciences, University of Edinburgh, Chancellor's Building, 49 Little France Crescent, Edinburgh UK Scotland EH16 4SB

Author contributions

JN carried out most of the experiments, including molecular biology, mouse surgeries, immunohistochemistry, slice imaging, RNA-seq, and behaviour with help from XY and BDC. XY performed analyses of RNA-seq. AB performed *in vivo* cortical calcium imaging experiments, including those surgeries. ZQ generated the AAV-PHP.eB viruses with guidance from VG, who provided equipment. SMS discussed iβARK with BSK at the germinal stages, shared reagents and insights. MO and MG helped with revision experiments. GC provided guidance on the analysis of RNA-seq data. PG supervised the *in vivo* imaging experiments. BSK conceived, designed, and directed the project, guided analyses, and performed electrophysiology. BSK and JN wrote the paper and all authors commented.

Declaration of Interests

The authors declare no competing interests relevant to this study. However, Baljit S. Khakh is a consultant for Third Rock.

Summary

Astrocytes respond to neurotransmitters and neuromodulators using G protein-coupled receptors (GPCRs) to mediate physiological responses. Despite their importance, there has been no method to genetically, specifically, and effectively attenuate astrocyte G_q GPCR pathways to explore consequences of this prevalent signaling mechanism *in vivo*. We report a 122 residue inhibitory peptide from β adrenergic receptor kinase 1 (iβARK and inactive D110A control) to attenuate astrocyte G_q GPCR signaling. iβARK significantly attenuated G_q GPCR Ca^{2+} signaling in brain slices and *in vivo*, altered behavioral responses, spared other GPCR responses, and did not alter astrocyte spontaneous Ca^{2+} signals, morphology, electrophysiological properties or gene expression in the striatum. Furthermore, brain wide attenuation of astrocyte G_q GPCR signaling with iβARK using PHP.eB AAVs, when combined with c-Fos mapping, suggested nucleispecific contributions to behavioral adaptation and spatial memory. iβARK extends the toolkit needed to explore functions of astrocyte G_q GPCR signaling within neural circuits *in vivo*.

eTOC Blurb

In this study, Nagai et al., report and carefully validate a genetic approach to attenuate astrocyte G_q GPCR signaling in the mouse brain *in vivo* with consequential effects on mouse behavior. The use of the method will enable new types of experiments in order to explore astrocytic contributions to neural circuit function and behavior and will be applicable broadly to open questions in neuroscience as well as in glial biology.

Graphical abstract

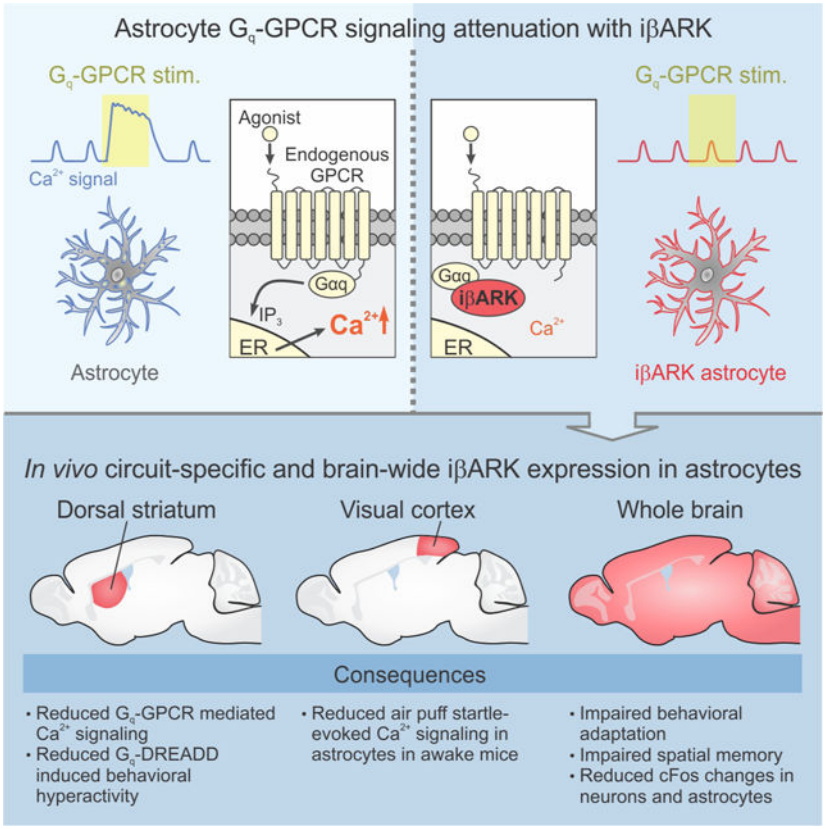

Introduction

Astrocytes tile the central nervous system and interact functionally and structurally with synapses and neurons within neural circuits during development and in a broad range of pathophysiological responses (Allen and Lyons, 2018; Molofsky and Deneen, 2015; Nagai et al., 2021). It has long been known that astrocytes express multiple G protein-coupled receptors (GPCRs), which allow them to sense neurotransmitters and neuromodulators in the extracellular space from local or long range projections (Fiacco et al., 2009; Kofuji and Araque, 2021b; Nimmerjahn and Bergles, 2015; Porter and McCarthy, 1997). An enduring goal has been to systematically explore and understand if, when, and how astrocytic GPCR signaling occurs and contributes to neural circuit and brain function.

Although pharmacological approaches targeting GPCRs provided a foundation for understanding astrocytic signaling, such approaches were stymied by the realization that astrocyte GPCRs also existed in multiple brain cell types, which complicated mechanistic studies (Fiacco et al., 2009; Khakh and McCarthy, 2015). To address these shortfalls, the last few years have witnessed progress with methods to activate astrocytes by using chemogenetic approaches such as Designer Receptors Exclusively Activated by Designer Drugs (DREADDs) to stimulate specific GPCR pathways (Roth, 2016). Although powerful such approaches also have some limitations. By virtue of the fact that signaling is exogenously activated, DREADDs often lack physiological context for the cellular responses, which in some cases makes it problematic to separate direct and secondary

contributions to complex responses and to behavior (Yu et al., 2020a). A second general limitation for astrocyte studies is that exogenous stimulation may not faithfully recapitulate endogenous pathways used *in vivo*, or may activate them in excess (Nagai et al., 2021). Although chemogenetics remains valuable to study astrocytes, such explorations would benefit from the availability of methods to attenuate defined types of ongoing GPCR activity within astrocytes as a complementary approach.

Astrocyte G_q coupled GPCR signaling and subsequent intracellular Ca^{2+} mobilization is engaged during behavioral stimuli such as startle and enforced locomotion (Bekar et al., 2008; Kim et al., 2016; Oe et al., 2020; Paukert et al., 2014; Ye et al., 2020), is altered in disease (Alvarez-Ferradas et al., 2015; Delekate et al., 2014; Reichenbach et al., 2018), and mediates cell-cell communication in some settings in neural circuits of rodents (Adamsky et al., 2018; Iwai et al., 2021; Kofuji and Araque, 2021b; Martin-Fernandez et al., 2017; Mederos et al., 2019; Otsu et al., 2015), fruit flies (Ma et al., 2016), zebrafish (Mu et al., 2019), and potentially in human astrocytes (Oberheim et al., 2009; Zhang et al., 2016). The functions of such signaling have begun to be explored by blocking Ca^{2+} release from intracellular stores by deleting inositol 1,4,5-trisphosphate type 2 receptors (IP_3R2) (Agulhon et al., 2010; Li et al., 2005), by buffering IP_3 (Xie et al., 2010) or by driving Ca^{2+} export out of the cell (Yu et al., 2018). These approaches have been insightful, but there are limitations. The use of IP_3R2 deletion mice initially suggested little evidence supporting a role for astrocyte IP_3-mediated Ca^{2+} signals in regulating behavior (Petravicz et al., 2014), but subsequent studies have found that such mice display altered responses (Kofuji and Araque, 2021a). The realization that IP_3R2 deletion mice show astrocyte Ca^{2+} signaling that was undetected in earlier studies has emphasized the need for additional methods to reduce astrocyte Ca^{2+} signaling (Di Castro et al., 2011; Rungta et al., 2016; Srinivasan et al., 2015; Stobart et al., 2018). Furthermore, astrocyte Ca^{2+} signals are now recognized to be diverse and existing approaches cannot discriminate between Ca^{2+} signals that derive from specific GPCR pathways and those resulting from additional Ca^{2+} signaling within astrocytes. General reduction of Ca^{2+} signaling also produced changes in gene expression (Yu et al., 2020b; Yu et al., 2018), which makes it harder to dissociate primary from secondary effects. Hence, there exists an unmet need to effectively attenuate – or "dial down" – G_q GPCR signaling specifically in astrocytes in order to explore astrocytic contributions to neural circuit function and behavior.

We report and carefully validate a genetic approach to attenuate astrocyte G_q GPCR signaling *in vivo*, which we expect will find broad applications in multiple experimental scenarios and open up new research directions to systematically explore fundamental astrocyte biology within neural circuits.

Results

Strategy for reducing G_q GPCR signaling

Upon agonist binding, G_q GPCRs initiate intracellular Ca^{2+} signaling by converting $G\alpha_q$-GDP to $G\alpha_q$-GTP, which induces phospholipase C (PLC)-dependent IP_3 generation and Ca^{2+} release from intracellular endoplasmic reticulum (ER) stores (Figure 1A). Extensive studies show that the regulator of G-protein signaling homology (RH) domain of GPCR

kinase 2 (GRK2)/β-adrenergic receptor kinase 1 (βARK1) (Evron et al., 2012) sequesters $G\alpha_q$-GTP (Carman et al., 1999; Sallese et al., 2000; Schumacher et al., 2016; Sterne-Marr et al., 2003; Usui et al., 2000) (Figure 1B), but not $G\alpha_q$-GDP, $G\alpha_{i/o}$, $G\alpha_s$, or $G\alpha_{12/13}$. Based on such studies, we envisioned that the 122 residue inhibitory peptide βARK-rgs (herein called iβARK) may selectively attenuate G_q GPCR-evoked Ca^{2+} signaling within astrocytes, which would be valuable given the physiological responses attributed to G_q GPCRs. We tested this idea and characterized iβARK in HEK-293 cells, as well as in astrocytes using Ca^{2+} imaging, immunohistochemistry (IHC), electrophysiology, chemogenetics, behavioral evaluations, and RNA-sequencing (RNA-seq).

We constructed mammalian expression vectors containing iβARK and mCherry (Figure 1C) to test the ability of iβARK to reduce G_q GPCR signaling in HEK-293 cells. We also engineered two additional constructs to express iβARK with point mutations to abolish $G\alpha_q$ binding: iβARK(R106A) and iβARK(D110A) (Sterne-Marr et al., 2004; Sterne-Marr et al., 2003). These were designed as negative controls for comparison with iβARK. Followingexpression in HEK-293 cells, we measured ATP-evoked Ca^{2+} responses mediated by endogenous G_q-coupled P2Y GPCRs (Figures 1D–F). In control cells expressing mCherry alone, ATP (50 μM) evoked robust Ca^{2+} responses. However, in cells expressing iβARK ATP-evoked responses were almost abolished (Figures 1D–F; n = 146–157 cells from 4 transfections per group, $P < 0.01$). Furthermore, cells expressing iβARK(R106A) and iβARK(D110A) mutants displayed ATP-evoked responses that were not different from the mCherry group (Figures 1D–F; 117–122 cells from 4 transfections, $P > 0.25$). Indeed, ATP-evoked responses from cells expressing iβARK(D110A) were indistinguishable from mCherry (Figure 1F), implying that the D110A mutant abolished the effect of iβARK. The ability of iβARK to block ATP-evoked responses, and the inability of iβARK(D110A) in these regards, was quantified at the level of single cells (Figure 1D), representative traces (Figure 1E), in the proportion of responding cells (Figure 1F), the average peak responses (Figure 1F), and across cell populations (Figure 1G). For subsequent evaluations following *in vivo* expression, we used iβARK in parallel with iβARK(D110A) as the mutant control. These constructs differ by one amino acid sidechain.

Reduction of astrocyte G_q GPCR signaling by iβARK *ex vivo*

Forexpression of iβARK and iβARK(D110A) within astrocytes *in vivo* (Figure 2A–B), we generated adeno-associated viruses (AAV2/5) with a 687 bp astrocyte-specific *GfaABC$_1$D* promoter (Shigetomi et al., 2013), mCherry, and a Woodchuck Hepatitis Virus Posttranscriptional Regulatory Element (WPRE; Figure 2A). Local microinjections into the dorsal striatum (dSTR) resulted in expression of iβARK and iβARK(D110A) AAVs in ~93% of S100β positive astrocytes (Figure 2B). No expression was detected in NeuN positive neurons (Figure 2B).

Astrocytes express a variety of GPCRs. We used Ca^{2+} imaging in brain slices to determine if iβARK reduced astrocyte G_q GPCR responses in somata and processes relative to iβARK(D110A) (Figure 2C–H). To this end, we expressed GCaMP6f along with iβARK mCherry or iβARK(D110A) mCherry in striatal astrocytes using astrocyte-selective AAVs (Chai et al., 2017). Phenylephrine (PE; 2 and 10 μM), an agonist of endogenously expressed

G_q-coupled α1-adrenoceptors (α1-ARs), evoked strong intracellular Ca^{2+} signaling in dSTR astrocytes (Yu et al., 2018) in the iβARK(D110A) group (Figure 2C). However, such responses were undetectable in most astrocytes expressing iβARK and on average iβARK attenuated the PE-evoked Ca^{2+} responses significantly by ~80% both in somata and processes (Figures 2C,G; Figure S3A). This was clear from the kymographs of individual astrocytes or their average traces (Figure 2C) and from the population data (Figure 2G). To assess if iβARK was similarly effective upon repetitive PE stimulation, we applied PE at 10 or 2 μM for 20 s, 5 times. We found significantly reduced responses for every PE application with iβARK relative to the control construct (Figure S1) indicating there was no tachyphylaxis in iβARK's effect with repeated PE applications. dSTR astrocyte Ca^{2+} responses mediated by G_i-coupled $GABA_B$ GPCRs activated with baclofen (50 μM, Figures S2A,C) and astrocyte Ca^{2+} responses evoked by ATP (50 μM) were unaffected by iβARK (Figures S2B,C).

We comment on ATP responses in dSTR astrocytes. First, we analyzed RNA-seq data (Chai et al., 2017) and found that dSTR astrocytes express ATP GPCRs that are $G_{i/o}$-coupled (Figure S2D, e.g. *P2y12, P2y13, P2y14*), while HEK-293 cells express mainly G_q-coupled P2Y receptors (Egan and Khakh, 2004; Fischer et al., 2005). Second, since ATP is degraded in seconds to adenosine in brain slices (Masino et al., 2002), we mined RNA-seq data to determine if dSTR astrocytes expressed adenosine receptors. This was the case; we found that G_i and G_s-coupled adenosine receptors displayed FPKM values of ~14 in dSTR astrocytes (Figure S2D), which is consistent with immunohistochemistry (Diaz-Castro et al., 2019). Third, to assess functional expression of adenosine receptors in dSTR astrocytes, we performed Ca^{2+} imaging with adenosine applications in the presence of TTX. Adenosine at 50 μM evoked large Ca^{2+} responses (Figure S2E). Our data suggest that ATP-evoked Ca^{2+} responses in dSTR astrocytes are mediated by a combination of $G_{i/o}$ -coupled P2Y and adenosine receptors, but not markedly by G_q-coupled P2Y receptors as in HEK-293 cells.

We performed a set of experiments to evaluate the specificity of iβARK to attenuate G_q GPCR mediated Ca^{2+} responses *versus* those mediated by G_i and G_s GPCRs in astrocytes. We employed clozapine-N-oxide (CNO) at 0.1 or 1 μM to activate hM3Dq (G_q), hM4Di (G_i), or rM3Ds (G_s) DREADDs (Chai et al., 2017; Roth, 2016) expressed in turn, but together with iβARK or iβARK(D110A). Consistent with the findings with endogenously expressed GPCRs reported above, we found that iβARK selectively blocked CNO-evoked G_q GPCR DREADD Ca^{2+} responses (Figures 2D,H), but not those mediated by G_i (Figures 2E,H) and G_s DREADDs (Figures 2F,H; n = 15–37 astrocytes from 4 mice for each condition per group, $P > 0.37$).

iβARK did not affect astrocyte spontaneous Ca^{2+} signals

Astrocytes display spontaneous Ca^{2+} signals that are independent of GPCR signaling (Shigetomi et al., 2016; Volterra et al., 2014). We discovered that such signals were unaltered in somata and processes by iβARK in terms of frequency, amplitude, and duration (Figure 3A–D, n = 18–32 astrocyte somata from 6 mice per group, $P > 0.30$). This result implies that iβARK selectively blocks only those signals mediated by G_q GPCR activation, which is an advantage over other strategies (Yu et al., 2020a). Thus, the CalEx approach

using a Ca^{2+} exporter, hPMCA2w/b, strongly attenuates all Ca^{2+} signals in astrocytes (Yu et al., 2021; Yu et al., 2018), and mice lacking intracellular IP_3R2s (*Itpr2*$^{-/-}$) display reduced spontaneous and GPCR mediated Ca^{2+} signals (Agulhon et al., 2010; Jiang et al., 2016; Srinivasan et al., 2015). In accord with these findings, we found that dSTR astrocyte spontaneous Ca^{2+} signals were strongly attenuated by CalEx (n = 10–20 astrocytes from 3–6 mice per group) and in *Itpr2*$^{-/-}$ mice (Figures 3A–C; n = 16–24 astrocytes from 4–6 mice per group). Of note, *Itpr2*$^{-/-}$ mice showed much reduced, but residual spontaneous Ca^{2+} signals in processes (Figure 3B–C) (Jiang et al., 2016; Srinivasan et al., 2015; Stobart et al., 2018). G_q GPCR evoked Ca^{2+} signals were also reduced in CalEx and *Itpr2*$^{-/-}$ mice (Figure S3B–E). Our data show preferential attenuation of astrocyte G_q GPCR responses by iβARK in relation to spontaneous Ca^{2+} signals.

iβARK effects on astrocyte morphology and electrophysiology were minimal

We assessed if iβARK affects astrocyte morphology and electrophysiological properties. Using Lck-GFP (Shigetomi et al., 2013), we evaluated astrocyte territory sizes, soma sizes, the numbers and widths of primary branches, and Feret's widths and lengths of whole astrocytes (Figures 3D and S4). Overall, we found no significant differences between iβARK and iβARK(D110A) groups (Figure 3D), except for slightly higher Lck-GFP intensity around the center of territories, possibly reflecting subtly increased width of primary branches in iβARK astrocytes (Figure S4). Electrophysiological properties (current-voltage relations, current waveforms, resting membrane potentials, membrane resistance) and Ba^{2+}-sensitive Kir4.1 currents between iβARK and iβARK(D110A) groups were not significantly different (Figure 3E).

iβARK did not markedly affect astrocyte gene expression

We determined if iβARK produced any other effects on astrocytes, because Ca^{2+} abrogation with CalEx and *Itpr2*$^{-/-}$ leads to altered gene expression (Yu et al., 2021; Yu et al., 2020b; Yu et al., 2018). We performed RNA-seq using the RiboTag AAV approach to selectively express Rpl22-HA in dSTR astrocytes (Diaz-Castro et al., 2019; Nagai et al., 2019; Yu et al., 2020b; Yu et al., 2018) in relation to all striatal cells (Figure S5A). We found that iβARK and iβARK(D110A) astrocytes were replete with 200 previously identified astrocyte enriched genes (Figure S5B) and expressed known prototypical astrocyte markers (*Aldh1l1*, *Aldoc*, *Slc1a2*, *Gja1*), but did not express markers of neurons, oligodendrocytes, microglia or endothelial cells (Figure S5C). We also examined expression of 38 genes proposed to identify reactive astrocytes (Liddelow et al., 2017), and found that none of them were altered in the iβARK group relative to iβARK(D110A). Consistent with the gene expression data, we also found no change in GFAP expression between iβARK and iβARK(D110A) groups (Figure S6). In contrast, several genes increased in control mice treated with LPS to induce reactivity (Figure S5D).

Next, we analyzed the RNA-seq data from iβARK and iβARK(D110A) astrocytes to determine if expression was altered for other genes (Figure 4). Strikingly, with a false discovery rate (FDR) < 0.05, only two genes were found to be differentially expressed with iβARK: *Snhg11* and *A330023F24Rik* (Figure 4A). In contrast, identical analyses showed several hundred genes were altered in CalEx or *Itpr2*−/− mice relative to controls (Yu et al.,

2020b) (Figure 4A). We also surveyed a panel of genes related to known astrocyte functions (Figure 4C). While a considerable number of genes were significantly altered in CalEx or *Itpr2−/−* astrocytes relative to their controls, no changes were found for iβARK astrocytes. Moreover, iβARK did not affect expression of genes encoding commonly studied GPCRs, G-proteins, and GPCR effectors and regulators (Figure 4D).

iβARK attenuated startle-evoked astrocyte Ca^{2+} signaling *in vivo*

Astrocyte G_q GPCR mediated Ca^{2+} signaling occurs in the somatosensory and visual cortex of mice when they are startled (Bekar et al., 2008; Kim et al., 2016; Oe et al., 2020; Paukert et al., 2014; Srinivasan et al., 2015; Srinivasan et al., 2016). The response is thought to be mediated by α1-adrenoceptors on astrocytes (Ye et al., 2020) that respond to endogenously released norepinephrine (NE) from locus coeruleus (LC) projections. We tested whether iβARK blocked this behavioral G_q GPCR response of astrocytes in awake mice. We microinjected iβARK and iβARK(D110A) AAVs along with GCaMP6f in the visual cortex of mice and subjected them to *in vivo* Ca^{2+} imaging using 2PLSM. iβARK and iβARK(D110A) were expressed in ~85% of S100β positive astrocytes in the visual cortex, and no significant expression was detected in NeuN positive neurons (Figure S7). Startle stimuli were elicited by a gentle puff of air to the face (Figures 5A–B). In iβARK(D110A) mice, we observed startle-evoked increases in astrocyte Ca^{2+} signaling in somata and processes (Figures 5C–E; n = 38 astrocytes, 3 mice). These data are presented as still frames before, during (0–5 s), and after (50–55 s) the startle in Figure 4C. However, startle-evoked Ca^{2+} signaling in astrocyte somata and processes was significantly attenuated in iβARK mice (Figures 5D–F; $P < 0.05$, n = 34 astrocytes, 4 mice). Consistent with brain slice work (Figures 3A–C), *in vivo* spontaneous Ca^{2+} signals were not affected by iβARK (Figures 5D,E,G; $P > 0.34$). We also tracked locomotion of the mice by recording paw movements. Paw movement was similar between iβARK and iβARK(D110A) groups (Figure 5H). Thus, *in vivo* imaging showed that iβARK strongly attenuated endogenous G_q GPCR mediated Ca^{2+} signaling in visual cortex astrocytes, even though the mice responded equivalently to the startle with increased movement.

iβARK rescued behavioral hyperactivity induced by G_q GPCR stimulation in dSTR astrocytes

dSTR astrocytes are implicated in behavioral hyperactivity with disrupted attention (Nagai et al., 2019). To determine how dSTR astrocyte G_q GPCR signaling affected behavior we deployed iβARK alone and together with G_q $hM3D_q$ DREADDs (Figure 6; Figure S8). We expressed iβARK or iβARK(D110A; Figure 6A) bilaterally in the dSTR in one experimental group called the “iβARK group” (Figures 6A–C). In a second group called the “$hM3D_q$ group”, we expressed $hM3D_q$ to stimulate G_q GPCR signaling (Figures 6D–F) and administered 1 mg/kg CNO or vehicle (i.p.) 2 hours before behavioral evaluations. In the iβARK group, locomotor activity and rearing in an open field arena were identical for iβARK and iβARK(D110A) (Figures 6B–C; 11–13 mice per group, $P > 0.05$). However, in the $hM3D_q$ group, CNO induced behavioral hyperactivity and increased rearing when compared to vehicle controls (Figures 6E–F; 8 mice per group, $P < 0.05$). Coincidentally, $hM3D_q$ mice did not display blunted responses to visual stimuli or to novel objects (Figures S8A,B; 8 mice per group, $P > 0.05$), implying hM3Dq activation elicited behavioral

responses separable to those reported for G_i GPCR signaling (Nagai et al., 2019). Moreover, there were no differences between iβARK and iβARK(D110A) mice to visual stimuli or novel objects (Figures S8C,D; 8 mice per group, $P > 0.05$).

We next asked if iβARK could block $hM3D_q$-evoked hyperactivity *in vivo*. We thus prepared a third group of mice with bilateral expression of $hM3D_q$ along with iβARK or iβARK(D110A), called the "hM3Dq + iβARK group" (Figures 6G–L). $hM3D_q$ + iβARK(D110A) + CNO mice displayed clear hyperactivity and increased rearing following CNO when compared to the iβARK(D110A) + CNO group (i.e. no $hM3D_q$) (Figures 6G–I; 8 mice per group, $P < 0.05$). This was in accord with data in Figure 6A–C and indicates that hyperactivity in $hM3D_q$ + iβARK(D110A) + CNO mice was not due to potential off target effects of CNO. In contrast, hyperactivity phenotypes were not observed in hM3Dq + iβARK + CNO mice (Figures 6J–L; 8 mice per group, $P > 0.05$). In the mice representing the hM3Dq + iβARK group, iβARK also significantly attenuated $hM3D_q$ mediated increased c-Fos expression within astrocytes relative to iβARK(D110A) (Figures S8E,F; 4 mice per group, $P = 0.029$). These results indicate that reducing dSTR astrocyte G_q pathway signaling does not affect spontaneous locomotion and rearing in an open field, while stimulating G_q GPCR pathways does so. Furthermore, iβARK significantly attenuated behavioral consequences of G_q DREADD pathway activation in astrocytes *in vivo* when compared to iβARK(D110A) and CNO controls (Figure 6).

Brain wide astrocyte selective attenuation of astrocyte G_q GPCR signaling

Although astrocyte G_q GPCR signaling has been widely discussed in the context of behaviorally relevant stimuli, astrocyte-neuron communication, and neurological diseases, it has proven problematic to explore *in vivo* roles for this signaling mechanism. Since G_q GPCR signaling exists in multiple brain areas, we deployed iβARK and iβARK(D110A) throughout the brain with AAV-PHP.eB viruses that are known to target brain cells (Chan et al., 2017; Ravindra Kumar et al., 2020) (Figures 7, 8, S9–12). It has been shown that expression within astrocytes using PHP.eB AAVs with a *GfaABC$_1$D* promoter was not widespread for some brain regions (Chan et al., 2017). Therefore, in this study we used the CAG promoter in a Cre-dependent PHP.eB in combination with astrocyte specific *Aldh1l1*-Cre/ER^{T2} mice (Srinivasan et al., 2016) (Figure 7A). This intersectional approach achieved brain wide astrocytic iβARK expression following AAV injections into the retro-orbital sinus (Challis et al., 2019) (Figures 7A–B). Following such injections, we assessed the astrocyte specificity of iβARK in 12 brain areas (Figure 7C) and found that 72–96% of S100β positive astrocytes were iβARK positive: we did not detect significant iβARK in NeuN positive neurons (Figures 7C and S9; n = 3 mice). To examine if iβARK was functional following expression by AAV-PHP.eB in *Aldh1l1*-Cre/ER^{T2} mice, we repeated Ca^{2+} imaging in dSTR astrocytes (Figure 7D). Consistent with Figure 2, iβARK-expressing cells showed significantly reduced PE-evoked Ca^{2+} signaling compared to iβARK(D110A) (Figure 7D; n = 20–21 astrocytes from 4 mice per group, $P < 0.001$).

Consequences of brain wide attenuation of astrocyte G_q GPCR signaling

Using AAV-PHP.eB vectors, we prepared mice expressing either iβARK or iβARK(D110A) and performed a SHIRPA behavioral screen to assess general changes in mouse health

and neurological function (Rogers et al., 1997) (Figure 8A). From the 44 assessments, we found that iβARK and iβARK(D110A groups were indiscernible for muscle, motor, sensory, autonomic, and spinocerebellar functions, and there was no evidence of overt neurological phenotypes assessed by SHIRPA (Figure 8A; 7–8 mice per group, $P > 0.05$), which recalls earlier observations (Petravicz et al., 2014). We should point out that with AAV-PHP.eB vectors in *Aldh1l1*-Cre/ER^{T2} mice, iβARK was also expressed in the kidney and liver, but not in the small intestine, lung, and heart (Figure S10; 3 mice per group, $P < 0.05$). However, we interpret the SHIRPA results to indicate that such expression did not produce overt changes and that the mice were healthy.

As a further validation of the iβARK approach to attenuate G_q GPCR signaling following brain wide expression, we assessed sensorimotor gating (Figures 8B–C). Mouse startle responses to acoustic pulses (120 dB for 20 ms) were reduced when a weaker pre-pulse (70, 75 or 80 dB for 20 ms) was given 100 ms prior to startle pulses, in a process called pre-pulse inhibition (PPI). iβARK and iβARK(D110A) groups showed similar PPI indicating no change in startle reflexes (Figures 8B–C; 8–10 mice per group, $P > 0.05$). However, when the mice were exposed to repetitive acoustic stimuli (120 dB for 20 ms, interval 10–30 s) for 1 hour (Figured 8D–F), iβARK mice displayed significantly distinct behavioral outcomes relative to iβARK(D110A). Both groups initially showed similar startle responses during the first 10 min (Figure 8E; 8–10 mice per group, $P = 0.97$), but over the ensuing hour iβARK(D110A) mice showed startle adaptation (i.e. a progressive decrease). In contrast, the iβARK mice showed no significant adaptation (Figures 8D,F; 8–10 mice per group, $P = 4.2 \times 10^{-4}$, Two-way ANOVA repeated measure). To explore the anatomical correlates of the responses underlying startle adaptation, the brains of mice were subjected to IHC for immediate early gene c-Fos in astrocytes and neurons (DeNardo and Luo, 2017) (Figures 8G–K, Figure S11) from brain areas thought to be associated with startle responses and adaptation (Sara, 2009, 2015; Sara and Bouret, 2012; Schwarz and Luo, 2015; Schwarz et al., 2015) (Figure 8G, Figure S11B). Significant startle adaptation-associated c-Fos upregulation was found in astrocytes from cortical and limbic areas receiving LC projections in the iβARK(D110A) control group (Figures 8G–I, Figures S11C–E; 4 mice per group, $P < 0.05$). In brain areas that are less innervated by LC projections such as the substantia nigra and the dorsal striatum, c-Fos expression did not change significantly in astrocytes (Figures 8J,K, Figure S11C–E; $P > 0.05$). In contrast to the iβARK(D110A) group, c-Fos upregulation was significantly reduced in iβARK mice (Figures 8J,K, Figure S11C–E; 4 mice per group, $P > 0.05$). Moreover, neurons also showed startle adaptation-associated c-Fos elevation in iβARK(D110A) mice (Figures 8J,K, Figures S11F–H; 4 mice per group, $P < 0.05$) and such neuronal c-Fos changes were significantly reduced in iβARK mice (Figures 8J,K, Figure S11F–H; 4 mice per group, $P > 0.05$). These results suggest that astrocyte G_q GPCR signaling contributes to neuronal activity resulting from startle-associated behavioral adaption. Moreover, mapping c-Fos expression in astrocytes and neurons suggested brain areas that may mediate such astrocyte-regulated responses.

Since the NE system contributes to learning and memory, we next performed tests to assess the consequences of astrocyte G_q GPCR signaling attenuation for cognitive function. Both iβARK and iβARK(D110A) groups performed similarly in contextual and cued fear-conditioned memory tests (Figure S12; 10–11 mice per group, $P > 0.05$), suggesting no

impact on long-term memory by iβARK. However, we found clear deficits in short-term spatial memory. In the Y-maze test, mice from iβARK and iβARK(D110A) groups freely explored and entered the three arms at similar levels (Figure 8L; 10–11 mice per group, $P = 0.43$). However, the iβARK(D110A) mice exhibited 63% successful rate of alternation, a task which requires working memory, while the iβARK group showed low alternation success (47%) below statistical chance at 50%. These data suggest deficits in spatial working memory in the iβARK mice (Figure 8L; 10–11 mice per group, $P = 4.5 \times 10^{-4}$). To further assess short-term spatial memory, we performed novel object placement tests. Although no difference was observed between groups for locomotion in the arena (Figure 8M; 10–11 mice per group, $P = 0.47$), the iβARK group did not respond to novel object placement (Figure 8M; 10–11 mice per group, $P = 6.2 \times 10^{-4}$), which supports altered short-term memory. Thus, brain wide attenuation of astrocyte G_q GPCR signaling with iβARK revealed several interesting behavioral phenotypes.

Discussion

Our goal in this study was to characterize and validate an approach to genetically attenuate astrocyte G_q GPCR signaling. iβARK can be used to selectively and cell-specifically reduce G_q GPCR signaling in astrocytes *in vivo* leading to specific behavioral alterations in mice without obvious deleterious effects on astrocytes. Our data indicate that astrocyte G_q GPCR signaling in the brain contributes to behavioral adaption and cognitive functions related to short term memory. The new genetic tools are useful for testing hypotheses regarding prevalent G_q GPCR signaling in local circuits through AAV microinjections or in the entire brain using PHP.eB AAVs.

Features of iβARK

A feature of iβARK compared with other astrocyte Ca^{2+} attenuation strategies is that it does not alter spontaneous Ca^{2+} signals and gene expression in astrocytes. The finding that iβARK did not alter astrocyte spontaneous Ca^{2+} signals is consistent with past studies (Jiang et al., 2016). Our empirical data are also in accord with the expectation that iβARK only binds to the active form of GTP-$G\alpha_q$ following agonist binding to GPCRs (Carman et al., 1999; Sallese et al., 2000; Sterne-Marr et al., 2003; Usui et al., 2000) and is not expected to directly affect ligand-independent functions of GPCRs, other GPCR pathways or unrelated sources of Ca^{2+}. In these regards, iβARK improves upon limitations of past Ca^{2+} attenuation approaches such as CalEx and *Itpr2*$^{-/-}$ mice. The data also show distinct cellular phenotypes in terms of spontaneous Ca^{2+} signaling between *Itpr2*$^{-/-}$ and iβARK astrocytes even though both IP_3Rs and $G\alpha_q$-GTP are involved in the G_q pathway. However, the deletion of IP_3R2s throughout development may constitutively alter intracellular Ca^{2+} mobilization besides the G_q pathway, such as potentially $G\beta\gamma$-mediated signaling by $G_{i/o}$ GPCRs in astrocytes that is also reliant on intracellular Ca^{2+} stores. Furthermore, the loss of IP_3R2s during development may have altered pathways involved in intracellular Ca^{2+} homeostasis such as Ca^{2+} entry and intracellular stores. Therefore, since IP_3R2s are downstream of $G\alpha_q$, the loss of Ca^{2+} signals observed in the IP_3R2 deletion mice are unlikely to be due to the inhibition of G_q-GPCR pathway alone, and several other pathways may conceivably contribute to the observed effects. The finding that astrocyte CalEx and IP_3R2 deletion resulted in altered

gene expression, whereas iβARK did not, emphasizes a feature of iβARK: it implies that any functional effects observed with iβARK are proximal to G_q GPCR signaling. More broadly, the data suggest the possibility that astrocyte transcriptomic profiles are regulated by ongoing spontaneous Ca^{2+} signaling and/or basal Ca^{2+} levels, and less so by agonist-activated G_q-GPCR pathway signaling.

By using brain wide iβARK delivery through an intersectional genetic approach, our proof-of-utility experiments suggest astrocytic contributions to behavioral adaptation and spatial memory, which are in line with recent reports (Adamsky et al., 2018; Iwai et al., 2021). Thus, chemogenetic and optogenetic stimulation of G_q GPCR pathways in hippocampal CA1 astrocytes are known to enhance contextual memory acquisition (Adamsky et al., 2018). Furthermore, optogenetic G_q GPCR pathway activation in astrocytes of the anterior cortex caused faster behavioral adaptation to novel environments (Iwai et al., 2021). Our c-Fos mapping data show that startle adaptation is accompanied with c-Fos changes in astrocytes and neurons within brain areas implicated in cognitive and adaptive behavior, such as the prefrontal cortex, hippocampus, and basolateral amygdala. c-Fos upregulation was significantly attenuated by astrocytic iβARK, illustrating the utility of the tool to explore functions of astrocytes within neural circuits and for mouse behavior. The current study did not explore the underlying synaptic mechanisms by which astrocyte G_q GPCR signaling modulates neuronal activity during behavioral adaptation and spatial memory. In future studies, several mechanisms need to be explored including potential release of neuromodulators, regulation of extracellular neurotransmitter and ion homeostasis, modulation of blood flow, and contributions to synapse formation and removal.

Considerations and areas for future improvement

iβARK did not completely inhibit G_q responses in astrocytes, especially those due to strong activation of G_q DREADDs. However, this may simply reflect that overexpression of DREADDs leads to strong responses that are larger than those with endogenous receptors; this will need to be assessed in future work. To further improve the efficacy of iβARK, there are three aspects to consider. First, G_q GPCRs activate not only $G\alpha_q$-mediated pathways, but also those due to $G\beta\gamma$, which iβARK does not block by its design. Second, with the currently available genetic strategies, iβARK expression may not be sufficiently high to bind to all available $G\alpha_q$-GTP. Third, iβARK may need to be localized to areas where $G\alpha_q$ exists within cells, such as by adding an appropriate targeting domain for more efficient spatial interactions between iβARK and $G\alpha_q$. Future studies also need to explore how iβARK blocks G_q signaling during more subtle stimulations, such as a during single neuron firing or during gentle touching of the whiskers in awake animals. Many ethologically innate behaviors should be explored.

Another consideration with the use of iβARK derives from the possibility that it may affect endogenous βARK1 functions (Penela et al., 2019). We emphasize that βARK1 is likely expressed at low levels in astrocytes (FPKM ~2 in the striatum). Our RNA-seq data from iβARK and iβARK(D110A)-expressing striatal astrocytes also showed no marked effects on gene expression (only two altered genes). Thus, transcripts for GPCRs, their regulators, and their downstream kinases were not altered by iβARK. This is in accord with studies

demonstrating the RH domain of βARK1 (iβARK) does not affect endogenous βARK1 functions including its kinase activity (Sterne-Marr et al., 2003). Nevertheless, in order to study the consequences of G_q GPCR signaling attenuation, iβARK should be used in parallel with iβARK(D110A) control. Our experiments also do not remove the need for further controls and orthogonal evaluations to assess specificity, efficacy, and downstream implications when iβARK is used in the future. Of course, iβARK is not a singular panacea and a diverse toolbox of reagents and approaches is needed to explore astrocytes. Additional strategies for inhibiting $G\alpha_q$ could be complementary to iβARK. For example, another potentially useful approach is to generate $G\alpha_q$-selective nanobodies, as has been done with $G\beta\gamma$-selective nanobodies (Gulati et al., 2018).

Examples of the uses of iβARK

There are immediate research areas where iβARK and iβARK(D110A) could be used for mechanistic studies. First, local microinjections of iβARK AAVs into specific brain areas will permit exploration of how astrocyte G_q GPCR signaling affects the multiple cells that astrocytes are known to interact with. Second, iβARK can be used in hypothesis-driven experiments to explore *in vivo* behavioral functions of astrocyte G_q GPCR signaling in brain regions where astrocytes are implicated (Nagai et al., 2021). Third, iβARK can be used to explore astrocyte contributions to neurovascular coupling. Fourth, iβARK could be used to determine if/how astrocyte G_q GPCR signaling regulates synaptogenesis. Fifth, iβARK will be valuable to assess how astrocyte G_q pathway signaling contributes to circuit dysfunctions in the context of diseases. Sixth, iβARK could be used to study morphogenesis and motility of astrocyte fine processes that are proposed to involve G_q signaling (Heller and Rusakov, 2015; Zhou et al., 2019). Dynamics of astrocyte processes relative to synapses could be studied by combining iβARK with the neuron-astrocyte proximity assay (Octeau et al., 2018). However, this is not feasible yet, because iβARK employs a red fluorescent protein that would interfere with the neuron-astrocyte proximity assay. Seventh, in the current study we analyzed astrocyte Ca^{2+} signals in somata and major processes of astrocytes. However, astrocyte Ca^{2+} signals are diverse in terms of their molecular basis and also in their observable spatiotemporal features such as the extent of spread and relationship between distinct events (Wang et al., 2019). Such spatiotemporal aspects have begun to be described, and merit exploration with iβARK. Finally, the genetic reagents we report may be used to express iβARK and iβARK(D110A) in other brain cells such as neurons, microglia, and oligodendrocytes.

In summary, iβARK extends study of astrocyte G_q GPCR signaling within brain slice preparations and *in vivo* and shows this mechanism is consequential for behavior. iβARK will be valuable to explore how astrocyte G_q GPCR signaling contributes to nervous system functions in different types of experimental scenarios of relevance to physiology, brain function, and disease.

STAR Methods

RESOURCE AVAILABILITY

Lead contact—Further information and requests for resources and reagents should be directed to and will be fulfilled by the Lead Contact, Baljit S. Khakh (bkhakh@mednet.ucla.edu).

Material availability statement—All unique/stable reagents generated in this study are available upon request from the Lead Contact without restriction. All of the new constructs generated in this study are also available from www.Addgene.org with IDs listed in the Key Resources Table.

Data and code availability—All data are available upon request from the Lead Contact. Raw RNA-seq data are provided in Excel file S1, and are deposited at the Gene Expression Omnibus (GEO# GSE158876). All statistics are reported in the figures and also provided in Excel file S1.

EXPERIMENTAL MODEL AND SUBJECT DETAILS

All animal experiments were conducted in accordance with the National Institute of Health Guide for the Care and Use of Laboratory Animals and were approved by the Chancellor's Animal Research Committee at the University of California, Los Angeles. All mice were housed with food and water available ad libitum in a 12 hr light/dark environment. All animals were healthy with no obvious behavioral phenotype, were not involved in previous studies, and were sacrificed during the light cycle.

Mouse models—Wild-type (WT) C57BL/6NJ mice were purchased from Jackson Laboratories and used after AAV surgeries at 6 weeks of age. *Aldh1l1*-Cre/ER^{T2} BAC transgenic mice (Jackson Laboratories, Stock # 029655) received AAV-PHP.eB viruses at 6–8 weeks of age for whole brain viral gene delivery. *Itpr2*$^{-/+}$ mice (Li et al., 2005) were originally generated by Ju chen (University of California, San Diego) and kindly gifted by Dr. Martin Paukert (University of Texas at San Antonio) and maintained as a heterozygous line. Homozygotes and WT littermates were used for AAV surgeries at 6 weeks of age. Data for experiments were collected from male and female adult mice (>P60). We used mice of both sexes in this study and did not analyze in detail sex-dependent effects as these were not of direct relevance to the generation and testing of the tools or to our specific scientific interests. However, we did not observe any noticeable differences between males and females during these experiments.

METHOD DETAILS

Generation of plasmid and AAV vector constructs—All plasmid constructs were generated using standard molecular biology techniques and the In-Fusion HD Cloning Kit (Clontech). All constructs were sequenced before use. Four plasmid constructs for cultured cells (CMV mCherry-WPRE, CMV iβARK-p2A-mCherry-WPRE [Addgene, #117688], CMV iβARK(R106A)-p2A-mCherry-WPRE [Addgene, #117689] and CMV iβARK(D110A)-p2A-mCherry-WPRE [Addgene, #117690]) were generated and

subsequently tested in HEK-293 cells. The iβARK-rgs coding sequence ggcgaggtgacttttgagaagatcttctcccagaagctggggtacctgcttttccgagacttctgcctgaagcacctggaggaggc caagcccttggtagagttctacgaggagatcaagaaatacgagaagctggagacagaggaggagcgcctggtctgcagccgaga gatctt cgccacgtacatcatgaaggagctgctggcctgctcacatcctttctcgaagagcgccattgagcacgtccagggccatctggtgaa gaag caggtgcctccggatctcttccagccatatattgaagaaatttgccagaacctccgaggagacgtgttccagaaattcatcgagagcg ataaa ttcaca (122 residue peptide; GEVTFEKIFSQKLGYLLFRDFCLKHLEEAKPLVEFYEEIKKYEKLETEEERLVCSREIF ATY IMKELLACSHPFSKSAIEHVQGHLVKKQVPPDLFQPYIEEICQNLRGDVFQKFIESDK FT) was provided by Dr. Walter J. Koch (Temple University) with a *NotI* restriction sites preceding the coding sequence of iβARK-rgs and an *XhoI* restriction site following the coding sequence. Together with a sequence encoding mCherry and WPRE that were amplified by PCR, iβARK-rgs was incorporated into pcDNA3.1 between *HindIII* and *XbaI* restriction sites, downstream of the CMV promoter. Single point mutations in the iβARK coding sequence were generated using QuikChange II Site-Directed Mutagenesis Kit (Agilent Technologies, #200523). For the two constructs (AAV2/5 *GfaABC$_1$D*-iβARK-p2A-mCherry-WPRE [Addgene, #117691], AAV2/5 *GfaABC$_1$D*-iβARK(D110A)-p2A-mCherry-WPRE [Addgene, #117692]), we modified plasmid pZac2.1 *GfaABC1D* Ezrin-GFP WPRE. We removed Ezrin-GFP using *EcoRI* and *AgeI* restriction enzymes and infused the iβARK constructs. We also created Cre-dependent (FLEx) expression vectors from pAAV CAG-FLEx-CyRFP1 (Addgene # 84357) by removing the CyRFP1 cDNA and infused iβARK (or iβARK[D110A])-p2A-mCherry-WPRE in an inverted orientation using the open *AscI* and *NheI* sites, creating the vectors CAG FLEx iβARK-p2A-mCherry-WPRE (Addgene, #117693) and CAG FLEx iβARK(D110A)-p2A-mCherry-WPRE (Addgene, #117694). The fully sequenced plasmids were sent to the UPenn Vector Core, which used them to generate AAV serotypes 2/5 for each construct (~2×10^{13} genome copies [GCs]/ml). All of our constructs have been deposited at Addgene in the Khakh lab repository for unrestricted distribution (http://www.addgene.org/Baljit_Khakh).

AAV-PHP.eB viruses—As described previously (Chan et al., 2017) AAV-PHP.eB:CAG-FLEx-iβARK-p2A-mCherry-WPRE and AAV-PHP.eB:CAG-FLEx-iβARK(D110A)-p2A-mCherry-WPRE were generated by triple transfection of HEK-293T cells (ATCC, CRL3216) using polyethylenimine (Polysciences, 23966–1). Viral particles were harvested from the medium at 72 h post transfection and from the cells and medium at 120 h. The cell pellets were lysed in SAN solution containing 500 mM NaCl, 40 mM Tris, 10 mM MgCl2, and 100 U/mL of salt-activated nuclease (Arcticzymes, 70900–202) at 37 °C for 1 h. Viral particles from the medium were precipitated with 8% polyethylene glycol (Sigma, 89510–1KG-F) in 500 mM NaCl, resuspended in SAN solution, and then combined with the cell lysates to incubate at 37 °C for another 30 min. Afterwards, the stocks were clarified by centrifugation at 2,000g and then purified over iodixanol (Optiprep, Cosmo Bio USA, AXS-1114542–5) density gradients (15%, 25%, 40% and 60%). Viruses were concentrated using Amicon filters (Millipore, UFC910024) and formulated in sterile PBS. Virus titers

were measured by determining the number of DNase I–resistant viral genome with qPCR using a linearized genome plasmid as a standard.

Transfections and imaging in cultured cells—Human embryonic kidney cells (HEK-293, ATCC) were maintained and used for imaging using standard procedures. In brief, HEK-293 cells were grown in DMEM/F12 media with Glutamax (Thermo Fisher Scientific) supplemented with 10% v/v fetal bovine serum and penicillin/streptomycin (100 units/ml). Cells were grown in a humidified cell culture incubator with 95% air / 5% CO_2 at 37 °C. Cells were prepared for transfection by plating onto 6-well plates at the time of splitting one day before transfection at 60–70% confluency. For transient expression in HEK-293, we used ~0.5 μg plasmid cDNA for expressing GCaMP6f along with mCherry, iβARK + mCherry, iβARK(R106A) + mCherry or iβARK(D110A) + mCherry. Constructs were transiently transfected using Effectene transfection reagent (QIAGEN) according to the manufacturer's instructions. Transfected cells were plated on poly-l-lysine coated coverslips. Coverslips were removed from DMEM/F12 media 40–64 hr post transfection, rinsed twice with HEK-293 cell imaging buffer (composition in mM: 150 NaCl, 1 CaCl2, 1 MgCl2, 10 glucose, 10 HEPES, pH 7.4 with NaOH) and placed into continuously perfused recording baths. Ca^{2+} signals were recorded under a laser-scanning confocal microscope (Olympus, FV1200) with a 40x water-immersion objective lens (NA 0.8) at 0.2 Hz. ATP (50 μM) was bath-applied in the recording solution for activating P2Y receptors endogenously expressed by HEK-293 cells.

AAV injection into the mouse brain—Surgical procedures for intracranial AAV2/5 microinjections have been described previously (Nagai et al., 2019; Yu et al., 2018). In brief, mice were anesthetized and placed onto a stereotaxic frame (David Kopf Instruments, Tujunga CA). Continuous anesthesia using isoflurane was carefully monitored and adjusted throughout the surgery. Mice were injected with buprenorphine (Buprenex; 0.1 mg/kg) subcutaneously before surgery. Scalp incisions were made and craniotomies (~1 mm in diameter) above the left parietal cortex were created using a high-speed drill (K.1070; Foredom) for unilateral viral injections while two craniotomies were made above both parietal cortices for bilateral viral injections. Beveled glass pipettes (1B100–4; World Precision Instruments) filled with viruses were placed into the dorsal striatum (0.8 mm anterior to the bregma, 2.0 mm lateral to the midline, and 2.4 mm from the pial surface). AAVs were injected at 200 nl/min using a syringe pump (Pump11 PicoPlus Elite; Harvard Apparatus). Glass pipettes were withdrawn after 10 min and scalps were cleaned and sutured with sterile surgical sutures. Mice were allowed to recover in clean cages with food containing Trimethoprim/Sulfamethoxazole and water for 7 days. Subsequent experiments were performed at least three weeks after surgeries. AAVs used in this study included: AAV2/5 *GfaABC$_1$D*-iβARK-p2A-mCherry-WPRE, AAV2/5 *GfaABC$_1$D*-iβARK(D110A)-p2A-mCherry-WPRE, AAV2/5 *GfaABC$_1$D*-Rpl22-HA (RiboTag AAV), AAV2/5 *GfaABC$_1$D*-PI-CRE, AAV2/5 *GfaABC$_1$D*-mCherry-hPMCA2w/b (CalEx AAV), AAV2/5 *GfaABC$_1$D*-hM3Dq-mCherry, AAV2/5 *GfaABC$_1$D*-GCaMP6f and AAV2/5 *GfaABC$_1$D*-Lck-GFP. All of these, except ones for expressing iβARK or iβARK(D110A), have been previously characterized for the striatum at the ages used in this study. Viruses were diluted with saline when necessary and injected with a total

volume of 0.5 μl per site to deliver ~0.5~1 × 10^{10} GCs into the dorsal striatum. To sparsely label astrocytes for morphological analysis, AAV2/5 *GfaABC$_1$D*-Lck-GFP was diluted to deliver 2 × 10^8 GCs.

Intravenous administration of AAV-PHP.eB: CAG-FLEx-iβARK-p2A-mCherry-WPRE or AAV-PHP.eB: CAG-FLEx-iβARK(D110A)-p2A-mCherry-WPRE (50 μl to deliver 10^{12} GCs per mouse) was performed by injection into the retro-orbital sinus of *Aldh1l1*-Cre/ER^{T2} BAC transgenic mice at 6–8 weeks of age. After 7–10 days allowing time for delivery, mice were intraperitoneally injected with 75 mg/kg tamoxifen dissolved in corn oil for 5 consecutive days and used for experiments at least 4 weeks after the last tamoxifen injection. For acute slice imaging, AAV2/5 *GfaABC$_1$D*-GCaMP6f was microinjected into the dorsal striatum as described in above at least three weeks before mice were sacrificed.

Immunohistochemistry (IHC) and analysis—For transcardial perfusion, mice were anesthetized with 5% isoflurane and once all reflexes subsided, the abdominal cavity was opened and heparin (50 units) was injected into the left ventricle to prevent blood coagulate. The animal was perfused with 20 ml ice cold 0.1 M phosphate buffered saline (PBS) followed by 60 ml 10% buffered formalin (Fisher #SF100–20). After gentle removal from the skull, the brain was post-fixed in 10% buffered formalin overnight at 4°C. The tissue was cryoprotected in 30% sucrose (0.1M PBS) and serial 40 μm coronal or 60 μm sagittal sections were prepared using a cryostat microtome (Leica) at −20°C and processed for immunohistochemistry. Sections were incubated with agitation in primary antibodies diluted in 0.1 M PBS with 0.5% Triton-X 100 for overnight at 4°C. The following primary antibodies were used: mouse anti-S100β (1:1,000; Sigma, S2532), rabbit anti-S100β (1:1,000; Abcam ab41548), mouse anti-NeuN (1:1,000; Millipore, MAB377), chicken anti-GFP (1:1,000; Abcam, ab13970), rabbit anti-RFP (1:1,000; Rockland, 600–401-379), or rabbit anti-cFos (1:5,000; Synaptic Systems, 226–003). The sections were then washed 3 times in 0.1 M PBS for 10 min each before incubation at room temperature for 2 hr with secondary antibodies diluted in 0.1 M PBS. Alexa conjugated (ThermoFisher Scientific) secondary antibodies were used at 1:1000 dilution. Fluorescent images were taken using UplanFL 40X 1.30 NA oil immersion objective lens on a confocal laser-scanning microscope (FV10-ASW; Olympus). Laser settings were kept the same within each experiment. Images were processed with ImageJ. Cell counting was done using the Cell Counter plugin. Intensity (immunoreactivity) measurements were performed using maximum intensity projections images. For the analysis of astrocyte territory size, the images of Lck-GFP-expressing astrocytes were thresholded to remove background signals. Images were then converted to a binary format in which pixels above the threshold were counted as 1 and pixels with signal at the level of background or lower were counted as 0. Astrocyte territory sizes were estimated by measuring the area of a ROI that surrounded the thresholded fluorescence profile of astrocytes.

Acute brain slice preparation for imaging and electrophysiology—Coronal striatal slices were prepared from adult (>P60) WT or *Aldh1l1*-Cre/ER^{T2} mice with AAV injection. Briefly, animals were deeply anesthetized with isoflurane and decapitated with sharp shears. The brains were placed and sliced in ice-cold modified artificial CSF (aCSF)

containing the following (in mM): 194 sucrose, 30 NaCl, 4.5 KCl, 1 MgCl2, 26 NaHCO3, 1.2 NaH2PO4, and 10 D-glucose, saturated with 95%O2 and 5%CO2. A vibratome (DSK-Zero1) was used to cut 300 mm brain sections. The slices were allowed to equilibrate for 30 min at 32–34°C in normal aCSF containing (in mM); 124 NaCl, 4.5 KCl, 2 CaCl2, 1 MgCl2, 26 NaHCO3, 1.2 NaH2PO4, and 10 D-glucose continuously bubbled with 95% O2 and 5% CO2. Slices were then stored at 21–23°C in the same buffer until use. All slices were used within 2–6 hours of slicing.

Electrophysiological recordings in the striatal slices—Electrophysiological recordings were performed using standard methods as described below. Slices were placed in the recording chamber and continuously perfused with 95% O2 and 5% CO2 bubbled normal aCSF at room temperature. pCLAMP10.4 software and a Multi-Clamp 700B amplifier was used for electrophysiology (Molecular Devices). Whole-cell patch-clamp recordings were made from astrocytes in the dorsolateral striatum using patch pipettes with a typical resistance of 5–6 MΩ. Astrocytes were morphologically and electrophysiologically identified and selected based on mCherry fluorescence. The intracellular solution comprised the following (in mM): 135 potassium gluconate, 5 KCl, 0.5 CaCl2, 5 HEPES, 5 EGTA, 2 Mg-ATP and 0.3 Na-GTP, pH 7.3 adjusted with KOH. To assess Ba^{2+}-sensitive Kir4.1 current, 300 μM $BaCl_2$ was applied in bath. Cells with access resistance that exceeded 20 MΩ were excluded from analysis. Analysis was performed using ClampFit 10.7 software.

Astrocyte intracellular Ca^{2+} imaging—Slice preparation was performed as described above. Cells for all the experiments were imaged using a Scientifica two-photon laser-scanning microscope (2PLSM) equipped with a MaiTai laser (Spectra-physics). To image GCaMP6f signals, laser was tuned at 920 nm wavelength. The laser power measured at the sample was less than 30 mW with a 40x water-immersion objective lens (Olympus). Astrocytes located in the dorsolateral striatum and typically ~20 to ~30 mm below the slice surface were selected for imaging. Images were acquired at 1 frame per second using SciScan software (Scientifica). Striatal slices were maintained in ACSF (124 mM NaCl, 4.5 mM KCl, 1 mM MgCl2, 1.2 mM NaH2PO4,26 mM NaHCO3, 10 mM D-glucose, and 2.0 mM CaCl2) through a perfusion system. Drug applications the following agonists of GPCRs were applied in the bath: Phenylephrine (PE, Tocris Bioscience 2838), Clozapine *N*-oxide (CNO, Tocris Bioscience 4936), ATP (Tocris Bioscience 3245) and (R)-Baclofen (Tocris Bioscience 0796). For a local application of drugs, a 5 s puff of 50 μM Adeonsine (Tocris Bioscience 3624) or 10 μM PE (Tocris Bioscience 2838) was administered via the PicoSpritzer III from Intracel. Tetrodotoxin (Cayman Chemical 14964) were applied in the bath at least 5 min prior to recording to allow adequate equilibration. A constant flow of fresh buffer perfused the imaging chamber at all times. Spontaneous Ca^{2+} signaling from CalEx and its parallel control (tdTomato) astrocytes were recorded for 3 min. In other conditions, we sometimes recorded for a longer time (~10 min). This does not affect the results, but in Figure 3C the data from the 3 min experiments appear more “layered”. Ca^{2+} signals were processed in ImageJ (NIH) and presented as the relative change in fluorescence (dF/F). Peak amplitude, half-width, frequency and integrated area of Ca^{2+} signals were analyzed in OriginPro 2016.

Head-bar installation, virus injection, and cranial window implantation—Wild type C57BL/6NJ mice were anesthetized with isoflurane (4% for induction, 1–1.5% vol/vol for maintenance) and placed in a stereotaxic frame (Kopf), with body temperature kept at ~37 °C with a feedback-controlled heating pad (Harvard Apparatus). After removing the scalp and clearing the skull of connective tissues, a custom-made lightweight metal head-bar was fixed onto the skull with cyanoacrylate adhesive (Krazy Glue) and covered with black dental cement (Ortho-Jet). A circular craniotomy (3-mm diameter) was then performed above the primary visual cortex V1 (centered at −2.5 mm lateral from lambda). With the skull opened and the dura intact, a viral cocktail containing AAV2/5 *GfaABC1D*-GCaMP6f plus AAV2/5 *GfaABC$_1$D*-iβARK-p2A-mCherry-WPRE or AAV2/5 *GfaABC$_1$D*-iβARK(D110A)-p2A-mCherry-WPRE was injected at two sites (1 μl each) near the center of the craniotomy, at a depth of 150–200 μm. 4 weeks after the injections, a glass cranial window consisting of a 3-mm diameter round #1 coverslip was implanted in the craniotomy, flush with the skull surface, and sealed in place using tissue adhesive (Vetbond). The exposed skull surrounding the cranial window was then completely covered with black dental cement to build a small chamber for imaging with a water-immersion objective. After surgery, animals were returned to their home cages at least 1 week for recovery and viral gene expression before subjecting to imaging experiments. Extreme care was taken to ensure that the dura experienced no damage or major bleeding before and after cranial window implantation. Mice with damaged dura or unclear window were discarded and not used for imaging experiments.

***In vivo* two-photon Ca^{2+} imaging, startle induction and mouse movement tracking—**Two-photon laser-scanning microscopy was performed with a moveable objective microscope (Thorlabs Mesoscope) using a Ti-Sapphire laser (Thorlabs Tiberius) at 920 nm, through a 0.6 NA water-immersion objective (Thorlabs). The objective was mounted at a tilt of 30 degrees to the vertical axis in order to image with the light path perpendicular to the cranial window and the cortical surface. Images were acquired using the ScanImage software (Vidrio Technologies) and processed with ImageJ (NIH). Fully awake mice, without any anesthesia, were mounted in a 2 inch diameter acrylic tube by securing its head-bar onto a custom-made head-bar holder under the microscope. Before experiments, mice were acclimated to the head fixation and to resting. Images were acquired every 100 ms (10 Hz) and downsampled to 1 Hz. Imaging was done with a resolution of at least 4 pixels/μm^2. Startle was induced by presenting a brief air puff to the face of the mice while the mice were resting in an acrylic tube during the imaging sessions. The air puff (~15 psi, 3 s) was delivered by opening a 2-way normally closed air pressure connected solenoid valve attached to a 1/8 inch PVC tubing with its opening positioned ~1 cm away from the nostril of the mice. Behavioral startle was confirmed by the locomotion induced immediately after presenting the air puff. To track the animal's movement, the animal's paw movement was recorded at 20 Hz with a Blackfly 2.3 monochromatic camera (BFLY-U323S6M-C). Using deep learning methods, a convolutional neural network was trained for detecting the animal's paw locations from which the animal's paw movement was then extracted. The motion data were acquired simultaneously with the Ca^{2+} imaging data and synchronized through the scanning mirror signals. The microscope was encased in a light-tight box, and the animals were kept in darkness without visible visual stimuli during the imaging sessions.

Mouse behavior—Behavioral tests were performed during the light cycle between 7:00 am and 7:00 pm. All the experimental mice were transferred to the behavior testing room at least 30 min before the tests to acclimatize to the environment and to reduce stress. Temperature and humidity of the experimental rooms were kept at 23 ± 2°C and 55 ± 5%, respectively. Background noise (65 ± 2 dB) was generated by white noise generator (San Diego Instruments) or Air Purifier 50150-N from Honeywell Enviracaire. 1 mg/kg CNO was intraperitoneally injected to mice in which $hM3D_q$ expressed in the dorsal striata 2 hours before the initiation of test.

Open field test: The open field chamber consisted of a square arena (28.7 × 30 cm) enclosed by walls made of translucent polyethylene (15 cm tall). The brightness of the experimental room was kept < 10 lux. Locomotor activity of mice was then recorded for 30 min using an infrared camera located above the open field chamber. Recording camera was connected to a computer operating an automated video tracking software ANY-maze from Stoelting or an automated video tracking software Topscan from CleverSys. Parameters analyzed included distance traveled with 5 and 30 min time bins.

Open field test with bright light stimulus: As previously described (Nagai et al., 2019), the modified open-field arena was a white, translucent polyethylene box (Model CB-80, Iris USA, Pleasant Prairie, WI) with internal dimensions of 69 cm long x 34 cm wide x 30 cm high. Three lamps containing single 100 W white light bulbs were positioned at one end of the table. One lamp was positioned 14 cm from the center of a short wall of the rectangular arena; one lamp flanked each long side of the arena, 14 cm from the long walls and 15 cm from the original short wall. All three lamps were situated 18 cm above the base of the arena. The test is divided into three phases. Illumination levels were measured with a light meter (Model 403125, Extech Instruments, Waltham, MA). Cameras suspended from the ceiling or floor monitored and captured activity of animals. Locomotive activity was measured using the software Topscan from CleverSys. Parameters analyzed included distance traveled in 4 min. Phase 1 minutes 1–4 is the dark phase where the lights are turned off (< 0.5 fc). Phase 2 is the light phase minutes 5–8 where the lights will be turned on and create an illumination gradient across the arena (~100 fc at one end of the open field with light). The change in locomotion was calculated as follows: distance traveled in Phase 1 divided by the distance traveled in Phase 2.

Rearing behavior: Mice were placed individually into plastic cylinders (15 cm in diameter and 35 cm tall) and allowed to habituate for 20 min. Rearing behavior was recorded and analyzed for 10 min. Number of bouts of rearing behavior, in which mice support their weight freely on its hind legs without using its tail or forepaws were manually counted.

Novel object recognition test: At day 1 and day 2, mice were placed in an empty open chamber (26.7 × 26.7 cm) for 10 minutes for habituation. At day 3 (training day), mice were placed in the same open chamber containing two identical objects evenly spaced apart; trial was video recorded for 10 minutes. At day 4 (testing day), 24 hours after training, mice were placed in the same open chamber, but one of the two objects has been replaced with a novel object; trial is video recorded for 10 minutes. Time exploring around the objects was

measured. Recognition index was calculated as follows: (time exploring the novel object – time exploring the familiar object) / (time exploring both objects) – 50.

SHIRPA primary behavioral screen: The primary screen was performed as previously described (Rogers et al., 1997). The standard method used provided a behavioral and functional profile by observational assessment of mice. The test aimed to examine defects in gait or posture, motor control and coordination, changes in excitability and aggression, salivation, lacrimation, piloerection, defecation, muscle tone, temperature and a gross measure of analgesia. All parameters were scored to provide a quantitative assessment, which enables comparison of results both over time and between different laboratories. The experiments were conducted by UCLA Behavioral Testing Core Facility and the investigators who performed experiments and analyses were blinded for mouse groups.

Behavioral observation: The primary screen provided a behavioral observation profile and assessment of each animal begins by observing undisturbed behavior in a viewing jar (clear Plexiglas cylinder, 11 cm diameter x 30 cm tall) for 5 min. In addition to the scored behaviors of body position, spontaneous activity, respiration rate, tremor, urination, and defecation, the observer logs any instances of bizarre or stereotyped behavior and convulsions, compulsive licking, self-destructive biting, retropulsion (walking backwards) and indications of spatial disorientation were assessed.

Arena behavior: A mouse was transferred to a clear Plexiglas arena (approximate internal dimensions 55 × 33 ×18 cm). In the floor of the arena, a Plexiglas sheet marked with 15 squares (11cm x 11 cm) was placed. Mice were tested for transfer arousal and observation of normal behavior. The arena was marked into a grid of 10 cm^2 squares to measure locomotor activity within a 30 s period. While the mouse is active in the arena, measures of palpebral closure, piloerection, startle response, gait, pelvic elevation, tail elevation, and touch escape are recorded. An IHR Click Box was used for testing the Preyer and startle responses. The Click Box generated a brief 20 KHz tone at 90 dB SPL when held 30cm above the mouse.

Above the arena: A sequence of manipulations using tail suspension and the grid across the width of the arena was performed. A grid with ~12 mm mesh was secured across the width of the box for measuring tail suspension and grip strength behavior. When held by the tail, measures of positional passivity, trunk curl, limb grasping, visual placing, whisker brush, and whisker placement were made.

Supine restraint: The animal was restrained in a supine position to record autonomic behaviors. During this assessment, grip strength, body tone, pinna reflex, corneal reflex, toe pinch, wire maneuver, body length, skin color, heart rate, limb tone, abdominal tone, lacrimation, salivation, provoked biting and penlight vision (pupil reflex) were evaluated. Cut lengths of 3 / 0 Mersilk held in the forceps was used for corneal and pinna reflex tests. A pair of dissecting equipment forceps, curved with fine points (125mm forceps, Philip Harris Scientific, Cat. No. D46–174), was used for the toe pinch. A rigid horizontal wire (3 mm diameter) is secured across the rear right corner such that the animals cannot touch the sides during the wire maneuver. A plastic dowel rod sharpened to a pencil point was used to test salivation and biting.

Balance and orientation: Several measures of vestibular system function were performed. The righting reflex, contact righting reflex, and negative geotaxis tests were performed. Throughout this procedure vocalization, urination and general fear, irritability, or aggression were recorded. A 30cm clear Plexiglas tube with an internal diameter of 2.5 cm was used for the contact righting reflex.

Pre-pulse inhibition and startle adaptation tests: Mice were placed in a Plexiglas cylinder (3.2 cm internal diameter) which was mounted on a sensor platform (SR-LAB-Startle Response System, San Diego Apparatus). Background white-noise (65 dB) generated by a standard speaker was delivered for 5 min before the initiation of test. Acoustic startle stimuli (120 dB, 20 ms) with or without pre-pulse stimuli (70, 75 or 80 dB, 20 ms) were delivered via a high frequency speaker, placed at a distance of 15 cm from the testing cylinder. For PPI test, mice were exposed to 6 startle presentations without pre-pulses, followed by the pseudo-randomized pre-pulse inhibition (PPI) trials where pre-pulse was delivered 100 ms before acoustic startle stimuli. For startle adaptation test, mice were exposed to 180 startle presentations without pre-pulses for 1 hour. Inter-trials intervals were randomized in the range of 10–30 s. The startle response was recorded by an accelerometer in the sensor platform and the peak amplitude was taken to be the maximal response occurring 100 ms following presentation of the acoustic startle stimulus. If mice showed activity above a certain threshold (>10 μV) at the start of the recording, data from the trials were removed because it could not be determined if recording was due to startle or spontaneously activity.

Pavlovian fear conditioning test: The fear conditioning apparatus (Med Associates) consisted of a conditioning chamber (29.5 × 23 × 20.5 cm), with a metal grid floor wired to a shock generator surrounded by an acoustic chamber (Med Associates), and controlled by the VideoFreeze software (Med Associates). Mice were placed in the conditioning chamber (approximately 75 lux) 3 min before the onset of the discrete conditioned stimulus (CS; 30 s, 2800 Hz, 75 dB tone). At the end of the CS, mice receive a short, mild foot shock unconditional stimulus (US; 0.75 mA, 2 s). Mice were exposed to three pairings of the CS and US, with an inter-trial interval of 1 min, and 60 s after the delivery of the third shock, mice were returned to their home cages. Conditioned fear was assessed by a continuous measurement of natural defense of freezing (lack of all movement except that required for respiration), the dominant behavioral fear response. Freezing was automatically measured throughout the testing trial by the VideoFreeze tracking software. To test contextual fear conditioning, mice were placed in the original conditioning box 24 hours (recent contextual fear memory) or 20 days (remote contextual fear memory) after the conditioning and freezing was recorded for 8 min. For measurements of auditory-cued fear conditioning, mice were placed in the same chamber with a novel context in terms of a cylinder-shaped cage on the walls, smooth floor, a different ambient scent, and ambient darkness at ~0 lux, where they are exposed to the same procedure as the training with the exception that there were no shocks. Freezing was assessed by the testing equipment during the different stages of the test (base line freezing to a novel context and inter-trial freezing).

Y-maze spontaneous alternation task test: To assess short-term memory of mice, Y maze in which three arms were placed at a natural angle (120 degrees) and assigned #1, #2 and #3 (Radial Arm Maze, Lafayette Instruments, arm length 30cm as measured from the door of the central area, arm width 10.5cm) was prepared. A mouse was placed into one of the arms and each trial began when the subject was in the centermost triangle between all three arms. Each trial ended when the subject's hind legs have crossed the threshold of the door of one of the arms. The arm the subject chose and the order of arm choice was recorded during a 7-minute session. To score the results, each set of 3 consecutive trials was examined for alternation such that all three arms were visited, and the total alternations was added up and divided by the total number of trials minus 2 (total number of possible alternations). For example, if a mouse chose the arm #3, #1, #2, #3, #2, #1 and #3 sequentially, 4 alternations / 5 possible alternations = 80% alternation.

Novel object placement test: At day 1, mice were placed in an empty open chamber (29 × 29 × 30 cm) for 10 minutes for habituation. At day 2, mice were placed in the same open chamber containing two identical objects evenly spaced apart; trial was video recorded for 10 minutes. At 1 hour later, mice were placed in the same open chamber, but one of the two objects has been replaced to different location; trial is video recorded for 10 minutes. Time exploring around the objects was measured. Descrimination index was calculated as follows: (time exploring the novel placement – time exploring the familiar placement) / (time exploring both placements) – 50.

Striatal astrocyte RNA-sequencing (RNA-seq) and analysis—To exact RNA from striatal astrocytes, RiboTag AAV along with AAV2/5 *GfaABC$_1$D*-iβARK-p2A-mCherry-WPRE or AAV2/5 *GfaABC$_1$D*-iβARK(D110A)-p2A-mCherry-WPRE was microinjected bilaterally into the dorsal striatum of mice at 6 weeks of age. Three weeks later, RNA was collected from striata of those mice (at 9 weeks of age). Briefly, striatal tissues were dissected and homogenized in ice-cold homogenization buffer. RNA was extracted from 10–20% of homogenate after centrifugation as input sample, which contained RNA from all cell types in the striatum (Qiagen Rneasy Plus Micro #74034). The remaining homogenate was incubated with mouse anti-HA antibody (1:250; Covance, #MMS-101R) for 4 hours at 4 °C followed by the addition of magnetic beads (Invitrogen, Dynabeads #110.04D) for overnight incubation at 4°C. RNA was purified from the immunoprecipitation (IP) sample, which contained astrocyte-enriched RNA (Qiagen RNeasy Plus Micro #74034). RNA concentration and quality were assessed with Agilent 2100 Bioanalyzer. RNA samples with RNA integrity number (RIN) greater than 7 were used for multiplexed library preparation with Nugen Ovation RNA-Seq System V2. For each experiment, all samples were multiplexed into a single pool in order to avoid batch effects (Auer and Doerge, 2010), and sequencing was performed on Illumina NextSeq 4000 for 2 × 75 yielding at least 45 million reads per sample. Demultiplexing was performed with Illumina Bcl2fastq2 v 2.17 program. Reads were aligned to the mouse mm10 reference genome using the STAR spliced read aligner with default parameters and fragment counts were derived using HTS-seq program. Approximately 70% of the reads mapped uniquely to the mouse genome and were used for subsequent analyses. Lowly expressed genes that had CPM > 3 in at least 4 samples were filtered out. Differential gene expression analysis was performed

with Bioconductor packages edgeR with false discovery rate (FDR) threshold < 0.05 (http://www.bioconductor.org). To represent the differential expression analyses of genes, expression level changes compared with the cognate control conditions [$\log_2$(Fold change)] and corresponding adjusted *P* values [-$\log_{10}$(*P* adj)] were used to construct the volcano plots. Astrocyte enrichment was calculated by fold-change of gene expression between IP samples and input samples from the control conditions. Genes with FPKM > 1 were selected for astrocyte function and GPCR signaling analyses. RNA-seq data from *Itpr2*$^{-/-}$ and CalEx mice were from RNA-seq data that we have previously made openly available (GSE143475 for *Itpr2*$^{-/-}$; GSE114757 for CalEx). To aid further assessments, RNA-seq data from mice received iβARK and iβARKD110A in dorsal striatal astrocytes has been deposited within the Gene Expression Omnibus (GEO) repository (https://www.ncbi.nlm.nih.gov/geo), accession ID # of GSE158876.

Imaging data analysis—Analyses of time lapse image series were performed using ImageJ (NIH). XY drift was corrected using ImageJ. Time traces of fluorescence intensity were extracted from the ROIs and converted to dF/F values. The somata were easy to identify and process ROIs were chosen to be within ~40 μm of the cell body. Processes were identified as the major branches emanating from the astrocyte soma. For analyzing spontaneous Ca^{2+} signaling, regions of interest (ROIs) were defined in normal aCSF (control). Using Origin 2016, Ca^{2+} events were manually marked. Event amplitudes, half width, event frequency per ROI per min, the integrated area-under-the-curve (AUC) of dF/F traces were measured using Origin. Events were identified based on amplitudes that were at least 2-fold above the baseline noise of the dF/F trace. Other than this, no other criteria were used.

QUANTIFICATION AND STATISTICAL ANALYSIS

Sample sizes were based on similar previously published work. The results of statistical comparisons, *n* numbers and *P* values are shown in the figure panels or figure legends with the average data. *N* is defined as the numbers of cells, sections or mice throughout on a case-by-case basis; the unit of analysis is stated in the text or in each figure legend. Full details of n numbers, precise *P* values, and statistical tests are reported in Excel file S1. When the average data are reported in the text, the statistics are reported there. Statistical tests were run in OriginPro 2016 or GraphPad Prism 8. Summary data are presented as mean ± SEM along with the individual data points. Note that in some of the graphs the bars representing the SEM in figure panels are smaller than the symbols used to represent the mean. For most statistical analyses we used non-parametric tests due to the sample sizes: two-tailed Mann–Whitney test for the comparisons between two groups and Kruskal-Wallis one-way ANOVA test followed by Dunn's *post hoc* test for the comparisons between more than two groups with significance declared at $P < 0.05$. For the Ca^{2+} imaging data, in order to avoid outcomes due to a nested design, a mixed effects model was used; specifically, we used nested t test for the comparisons between two groups or a nested one-way ANOVA test for the comparisons between more than two groups (GraphPad Prism 8). In the figures, *P* values were indicated by asterisk(s): *, $P < 0.05$; **, $P < 0.01$; ***, $P < 0.001$; ****, $P < 0.0001$. A statistical FDR value < 0.05 was used for all RNA-seq analyses. All mice were

assigned to particular experimental groups at random. No data points were excluded from any experiment.

Supplementary Material

Refer to Web version on PubMed Central for supplementary material.

Acknowledgments

We thank the UCLA Neuroscience Genomics Core for assistance with sequencing, and Fuying Gao for helping with data analysis. Thanks to UCLA Behavioral Testing Core for guidance and equipment. Collaborations between the BSK and VG groups are supported by the NIH grant DA047444. Supported by the National Institutes of Health (R35NS111583), by an Allen Distinguished Investigator Award through The Paul G. Allen Frontiers Group, and by the Ressler Family Foundation (BSK). SMS was supported by the Brody Family Medical Trust Fund Fellowship and NIH grant HL 132882. JN was partly supported by a JSPS Overseas Research Fellowship (H28-729) and the Uehara Memorial Foundation Overseas Postdoctoral Research Fellowship (201730082). XY was partly supported by the American Heart Association (16POST27260256). We acknowledge the NINDS Informatics Center for Neurogenetics and Neurogenomics (P30 NS062691 to GC) and the Genetics, Genomics and Informatics Core of the Semel Institute of Neuroscience at UCLA (U54HD087101-01 from the Eunice Kennedy Shriver National Institute of Child Health and Human Development). PG and AB were supported by R01NS116589. VG was supported by a NIH Pioneer Award (DP1OD025535), the Vallee Foundation, the CZI Neurodegeneration Challenge Network, and the Beckman Institute for CLARITY, Optogenetics and Vector Engineering Research (CLOVER) for technology development and dissemination.

References

Adamsky A, Kol A, Kreisel T, Doron A, Ozeri-Engelhard N, Melcer T, Refaeli R, Horn H, Regev L, Groysman M, et al. (2018). Astrocytic Activation Generates De Novo Neuronal Potentiation and Memory Enhancement. Cell 174, 59–71 e14. [PubMed: 29804835]

Agulhon C, Fiacco TA, and McCarthy KD (2010). Hippocampal short- and long-term plasticity are not modulated by astrocyte Ca2+ signaling. Science 327, 1250–1254. [PubMed: 20203048]

Allen NJ, and Lyons DA (2018). Glia as architects of central nervous system formation and function. Science 362, 181–185. [PubMed: 30309945]

Alvarez-Ferradas C, Morales JC, Wellmann M, Nualart F, Roncagliolo M, Fuenzalida M, and Bonansco C. (2015). Enhanced astroglial Ca2+ signaling increases excitatory synaptic strength in the epileptic brain. Glia63, 1507–1521. [PubMed: 25980474]

Bekar LK, He W, and Nedergaard M. (2008). Locus coeruleus alpha-adrenergic-mediated activation of cortical astrocytes in vivo. Cereb Cortex18, 2789–2795. [PubMed: 18372288]

Carman CV, Parent JL, Day PW, Pronin AN, Sternweis PM, Wedegaertner PB, Gilman AG, Benovic JL, and Kozasa T. (1999). Selective regulation of Galpha(q/11) by an RGS domain in the G protein-coupled receptor kinase, GRK2. J Biol Chem274, 34483–34492. [PubMed: 10567430]

Chai H, Diaz-Castro B, Shigetomi E, Monte E, Octeau JC, Yu X, Cohn W, Rajendran PS, Vondriska TM, Whitelegge JP, et al. (2017). Neural circuit-specialized astrocytes: transcriptomic, proteomic, morphological, and functional evidence. Neuron 95, 531–549. [PubMed: 28712653]

Challis RC, Ravindra Kumar S, Chan KY, Challis C, Beadle K, Jang MJ, Kim HM, Rajendran PS, Tompkins JD, Shivkumar K, et al. (2019). Systemic AAV vectors for widespread and targeted gene delivery in rodents. Nat Protoc 14, 379–414. [PubMed: 30626963]

Chan KY, Jang MJ, Yoo BB, Greenbaum A, Ravi N, Wu WL, Sanchez-Guardado L, Lois C, Mazmanian SK, Deverman BE, et al. (2017). Engineered AAVs for efficient noninvasive gene delivery to the central and peripheral nervous systems. Nat Neurosci 20, 1172–1179. [PubMed: 28671695]

Delekate A, Fuchtemeier M, Schumacher T, Ulbrich C, Foddis M, and Petzold GC (2014). Metabotropic P2Y1 receptor signalling mediates astrocytic hyperactivity in vivo in an Alzheimer's disease mouse model. Nat Commun 5, 5422. [PubMed: 25406732]

DeNardo L, and Luo L. (2017). Genetic strategies to access activated neurons. Curr Opin Neurobiol45, 121–129. [PubMed: 28577429]

Di Castro MA, Chuquet J, Liaudet N, Bhaukaurally K, Santello M, Bouvier D, Tiret P, and Volterra A. (2011). Local Ca2+ detection and modulation of synaptic release by astrocytes. Nat Neurosci10, 1276–1284.

Diaz-Castro B, Gangwani MR, Yu X, Coppola G, and Khakh BS (2019). Astrocyte molecular signatures in Huntington's disease. Sci Transl Med 11, eaaw8546.

Egan TM, and Khakh BS (2004). Contribution of calcium ions to P2X channel responses. J Neurosci 24, 3413–3420. [PubMed: 15056721]

Evron T, Daigle TL, and Caron MG (2012). GRK2: multiple roles beyond G protein-coupled receptor desensitization. Trends Pharmacol Sci 33, 154–164. [PubMed: 22277298]

Fiacco TA, Agulhon C, and McCarthy KD (2009). Sorting out astrocyte physiology from pharmacology. Annu Rev Pharmacol Toxicol 49, 151–174. [PubMed: 18834310]

Fischer W, Franke H, Groger-Arndt H, and Illes P. (2005). Evidence for the existence of P2Y1,2,4 receptor subtypes in HEK-293 cells: reactivation of P2Y1 receptors after repetitive agonist application. Naunyn Schmiedebergs Arch Pharmacol371, 466–472. [PubMed: 16025270]

Gulati S, Jin H, Masuho I, Orban T, Cai Y, Pardon E, Martemyanov KA, Kiser PD, Stewart PL, Ford CP, et al. (2018). Targeting G protein-coupled receptor signaling at the G protein level with a selective nanobody inhibitor. Nat Commun 9, 1996. [PubMed: 29777099]

Heller JP, and Rusakov DA (2015). Morphological plasticity of astroglia: Understanding synaptic microenvironment. Glia 63, 2133–2151. [PubMed: 25782611]

Iwai Y, Ozawa K, Yahagi K, Mishima T, Akther S, Vo CT, Lee AB, Tanaka M, Itohara S, and Hirase H. (2021). Transient Astrocytic Gq Signaling Underlies Remote Memory Enhancement. Front Neural Circuits15, 658343.

Jiang R, Diaz-Castro B, Looger LL, and Khakh BS (2016). Dysfunctional calcium and glutamate signaling in striatal astrocytes from huntington's disease model mice. J Neurosci 36, 3453–3470. [PubMed: 27013675]

Khakh BS, and McCarthy KD (2015). Astrocyte calcium signaling: from observations to functions and the challenges therein. Cold Spring Harb Perspect Biol 1 20;7(4):a020404. doi: 10.1101/cshperspect.a020404.

Kim SK, Hayashi H, Ishikawa T, Shibata K, Shigetomi E, Shinozaki Y, Inada H, Roh SE, Kim SJ, Lee G, et al. (2016). Cortical astrocytes rewire somatosensory cortical circuits for peripheral neuropathic pain. J Clin Invest 126, 1983–1997. [PubMed: 27064281]

Kofuji P, and Araque A. (2021a). Astrocytes and Behavior. Annu Rev Neurosci in press; 10.1146/annurev-neuro-101920-112225.

Kofuji P, and Araque A. (2021b). G-Protein-Coupled Receptors in Astrocyte-Neuron Communication. Neuroscience456, 71–84. [PubMed: 32224231]

Li X, Zima AV, Sheikh F, Blatter LA, and Chen J. (2005). Endothelin-1-induced arrhythmogenic Ca2+ signaling is abolished in atrial myocytes of inositol-1,4,5-trisphosphate(IP3)-receptor type 2-deficient mice. Circulation research96, 1274–1281. [PubMed: 15933266]

Liddelow SA, Guttenplan KA, Clarke LE, Bennett FC, Bohlen CJ, Schirmer L, Bennett ML, Munch AE, Chung WS, Peterson TC, et al. (2017). Neurotoxic reactive astrocytes are induced by activated microglia. Nature 541, 481–487. [PubMed: 28099414]

Ma Z, Stork T, Bergles DE, and Freeman MR (2016). Neuromodulators signal through astrocytes to alter neural circuit activity and behaviour. Nature 539, 428–432. [PubMed: 27828941]

Martin-Fernandez M, Jamison S, Robin LM, Zhao Z, Martin ED, Aguilar J, Benneyworth MA, Marsicano G, and Araque A. (2017). Synapse-specific astrocyte gating of amygdala-related behavior. Nat Neurosci20, 1540–1548. [PubMed: 28945222]

Masino SA, Diao L, Illes P, Zahniser NR, Larson GA, Johansson B, Fredholm BB, and Dunwiddie TV (2002). Modulation of hippocampal glutamatergic transmission by ATP is dependent on adenosine a(1) receptors. The Journal of pharmacology and experimental therapeutics 303, 356–363. [PubMed: 12235271]

Mederos S, Hernandez-Vivanco A, Ramirez-Franco J, Martin-Fernandez M, Navarrete M, Yang A, Boyden ES, and Perea G. (2019). Melanopsin for precise optogenetic activation of astrocyte-neuron networks. Glia67, 915–934. [PubMed: 30632636]

Molofsky AV, and Deneen B. (2015). Astrocyte development: A Guide for the Perplexed. Glia63, 1320–1329. [PubMed: 25963996]

Mu Y, Bennett DV, Rubinov M, Narayan S, Yang CT, Tanimoto M, Mensh BD, Looger LL, and Ahrens MB (2019). Glia Accumulate Evidence that Actions Are Futile and Suppress Unsuccessful Behavior. Cell 178, 27–43 e19. [PubMed: 31230713]

Nagai J, Rajbhandari AK, Gangwani MR, Hachisuka A, Coppola G, Masmanidis SC, Fanselow MS, and Khakh BS (2019). Hyperactivity with Disrupted Attention by Activation of an Astrocyte Synaptogenic Cue. Cell 177, 1280–1292 e1220. [PubMed: 31031006]

Nagai J, Yu X, Papouin T, Cheong E, Freeman MR, Monk KR, Hastings MH, Haydon PG, Rowitch D, Shaham S, et al. (2021). Behaviorally consequential astrocytic regulation of neural circuits. Neuron 109, 576–596. [PubMed: 33385325]

Nimmerjahn A, and Bergles DE (2015). Large-scale recording of astrocyte activity. Curr Opin Neurobiol 32, 95–106. [PubMed: 25665733]

Oberheim NA, Takano T, Han X, He W, Lin JH, Wang F, Xu Q, Wyatt JD, Pilcher W, Ojemann JG, et al. (2009). Uniquely hominid features of adult human astrocytes. J Neurosci 29, 3276–3287. [PubMed: 19279265]

Octeau JC, Chai H, Jiang R, Bonanno SL, Martin KC, and Khakh BS (2018). An Optical Neuron-Astrocyte Proximity Assay at Synaptic Distance Scales. Neuron 98, 49–66. [PubMed: 29621490]

Oe Y, Wang X, Patriarchi T, Konno A, Ozawa K, Yahagi K, Hirai H, Tian L, McHugh TJ, and Hirase H. (2020). Distinct temporal integration of noradrenaline signaling by astrocytic second messengers during vigilance. Nat Commun11, 471. [PubMed: 31980655]

Otsu Y, Couchman K, Lyons DG, Collot M, Agarwal A, Mallet JM, Pfrieger FW, Bergles DE, and Charpak S. (2015). Calcium dynamics in astrocyte processes during neurovascular coupling. Nat Neurosci18, 210–218. [PubMed: 25531572]

Paukert M, Agarwal A, Cha J, Doze VA, Kang JU, and Bergles DE (2014). Norepinephrine controls astroglial responsiveness to local circuit activity. Neuron 82, 1263–1270. [PubMed: 24945771]

Penela P, Ribas C, Sánchez-Madrid F, and Mayor F Jr. (2019). G protein-coupled receptor kinase 2 (GRK2) as a multifunctional signaling hub. Cellular and molecular life sciences : CMLS 76, 4423–4446. [PubMed: 31432234]

Petravicz J, Boyt KM, and McCarthy KD (2014). Astrocyte IP3R2-dependent Ca(2+) signaling is not a major modulator of neuronal pathways governing behavior. Front Behav Neurosci 11 12;8:384. doi: 10.3389/fnbeh.2014.00384. eCollection 2014. [PubMed: 25429263]

Porter JT, and McCarthy KD (1997). Astrocytic neurotransmitter receptors in situ and in vivo. Prog Neurobiol 51, 439–455. [PubMed: 9106901]

Ravindra Kumar S, Miles TF, Chen X, Brown D, Dobreva T, Huang Q, Ding X, Luo Y, Einarsson PH, Greenbaum A, et al. (2020). Multiplexed Cre-dependent selection yields systemic AAVs for targeting distinct brain cell types. Nat Methods 17, 541–550. [PubMed: 32313222]

Reichenbach N, Delekate A, Breithausen B, Keppler K, Poll S, Schulte T, Peter J, Plescher M, Hansen JN, Blank N, et al. (2018). P2Y1 receptor blockade normalizes network dysfunction and cognition in an Alzheimer's disease model. J Exp Med 215, 1649–1663. [PubMed: 29724785]

Rogers DC, Fisher EM, Brown SD, Peters J, Hunter AJ, and Martin JE (1997). Behavioral and functional analysis of mouse phenotype: SHIRPA, a proposed protocol for comprehensive phenotype assessment. Mamm Genome 8, 711–713. [PubMed: 9321461]

Roth BL (2016). DREADDs for neuroscientists. Neuron 89, 683–694. [PubMed: 26889809]

Rungta R, Bernier L-P, Dissing-Olesen L, Groten C, LeDue J, Drissler S, and MacVicar B. (2016). Ca2+ transients in astrocyte fine processes occur via Ca2+ influx in adult mouse hippocampus. Glia64, 2093–2103. [PubMed: 27479868]

Sallese M, Mariggio S, D'Urbano E, Iacovelli L, and De Blasi A. (2000). Selective regulation of Gq signaling by G protein-coupled receptor kinase 2: direct interaction of kinase N terminus with activated galphaq. Mol Pharmacol57, 826–831. [PubMed: 10727532]

Sara SJ (2009). The locus coeruleus and noradrenergic modulation of cognition. Nat Rev Neurosci 10, 211–223. [PubMed: 19190638]

Sara SJ (2015). Locus Coeruleus in time with the making of memories. Curr Opin Neurobiol 35, 87–94. [PubMed: 26241632]

Sara SJ, and Bouret S. (2012). Orienting and reorienting: the locus coeruleus mediates cognition through arousal. Neuron76, 130–141. [PubMed: 23040811]

Schumacher SM, Gao E, Cohen M, Lieu M, Chuprun JK, and Koch WJ (2016). A peptide of the RGS domain of GRK2 binds and inhibits Galpha(q) to suppress pathological cardiac hypertrophy and dysfunction. Science signaling 9, ra30.

Schwarz LA, and Luo L. (2015). Organization of the locus coeruleus-norepinephrine system. Curr Biol25, R1051–R1056. [PubMed: 26528750]

Schwarz LA, Miyamichi K, Gao XJ, Beier KT, Weissbourd B, DeLoach KE, Ren J, Ibanes S, Malenka RC, Kremer EJ, et al. (2015). Viral-genetic tracing of the input-output organization of a central noradrenaline circuit. Nature 524, 88–92. [PubMed: 26131933]

Shigetomi E, Bushong EA, Haustein MD, Tong X, Jackson-Weaver O, Kracun S, Xu J, Sofroniew MV, Ellisman MH, and Khakh BS (2013). Imaging calcium microdomains within entire astrocyte territories and endfeet with GCaMPs expressed using adeno-associated viruses. The Journal of general physiology 141, 633–647. [PubMed: 23589582]

Shigetomi E, Patel S, and Khakh BS (2016). Probing the Complexities of Astrocyte Calcium Signaling. Trends Cell Biol 26, 300–312. [PubMed: 26896246]

Srinivasan R, Huang BS, Venugopal S, Johnston AD, Chai H, Zeng H, Golshani P, and Khakh BS (2015). Ca(2+) signaling in astrocytes from Ip3r2(−/−) mice in brain slices and during startle responses in vivo. Nat Neurosci 18, 708–717. [PubMed: 25894291]

Srinivasan R, Lu TY, Chai H, Xu J, Huang BS, Golshani P, Coppola G, and Khakh BS (2016). New Transgenic Mouse Lines for Selectively Targeting Astrocytes and Studying Calcium Signals in Astrocyte Processes In Situ and In Vivo. Neuron 92, 1181–1195. [PubMed: 27939582]

Sterne-Marr R, Dhami GK, Tesmer JJ, and Ferguson SS (2004). Characterization of GRK2 RH domain-dependent regulation of GPCR coupling to heterotrimeric G proteins. Methods Enzymol 390, 310–336. [PubMed: 15488186]

Sterne-Marr R, Tesmer JJ, Day PW, Stracquatanio RP, Cilente JA, O'Connor KE, Pronin AN, Benovic JL, and Wedegaertner PB (2003). G protein-coupled receptor kinase 2/G alpha q/11 interaction. A novel surface on a regulator of G protein signaling homology domain for binding G alpha subunits. J Biol Chem 278, 6050–6058. [PubMed: 12427730]

Stobart JL, Ferrari KD, Barrett MJP, Gluck C, Stobart MJ, Zuend M, and Weber B. (2018). Cortical circuit activity evokes rapid astrocyte calcium signals on a similar timescale to neurons. Neuron98, 726–735. [PubMed: 29706581]

Usui H, Nishiyama M, Moroi K, Shibasaki T, Zhou J, Ishida J, Fukamizu A, Haga T, Sekiya S, and Kimura S. (2000). RGS domain in the amino-terminus of G protein-coupled receptor kinase 2 inhibits Gq-mediated signaling. Int J Mol Med5, 335–340. [PubMed: 10719047]

Volterra A, Liaudet N, and Savtchouk I. (2014). Astrocyte Ca(2)(+) signalling: an unexpected complexity. Nat Rev Neurosci15, 327–335. [PubMed: 24739787]

Wang Y, DelRosso NV, Vaidyanathan TV, Cahill MK, Reitman ME, Pittolo S, Mi X, Yu G, and Poskanzer KE (2019). Accurate quantification of astrocyte and neurotransmitter fluorescence dynamics for single-cell and population-level physiology. Nat Neurosci 22, 1936–1944. [PubMed: 31570865]

Xie Y, Wang T, Sun GY, and Ding S. (2010). Specific disruption of astrocytic Ca2+ signaling pathway in vivo by adeno-associated viral transduction. Neuroscience170, 992–1003. [PubMed: 20736051]

Ye L, Orynbayev M, Zhu X, Lim EY, Dereddi RR, Agarwal A, Bergles DE, Bhat MA, and Paukert M. (2020). Ethanol abolishes vigilance-dependent astroglia network activation in mice by inhibiting norepinephrine release. Nat Commun11, 6157. [PubMed: 33268792]

Yu X, Moye SL, and Khakh BS (2021). Local and CNS-wide astrocyte intracellular caclium signlaing attenuation in vivo with CalExflox mice. J Neurosci in press.

Yu X, Nagai J, and Khakh BS (2020a). Improved tools to study astrocytes. Nat Rev Neurosci 21, 121–138. [PubMed: 32042146]

Yu X, Nagai J, Marti-Solano M, Soto JS, Coppola G, Babu MM, and Khakh BS (2020b). Context-specific striatal astrocyte molecular responses are phenotypically exploitable. Neuron 10 9;S0896–6273(20)30745–5. doi: 10.1016/j.neuron.2020.09.02.

Yu X, Taylor AMW, Nagai J, Golshani P, Evans CJ, Coppola G, and Khakh BS (2018). Reducing Astrocyte Calcium Signaling In Vivo Alters Striatal Microcircuits and Causes Repetitive Behavior. Neuron 99, 1170–1187 e1179. [PubMed: 30174118]

Zhang Y, Sloan SA, Clarke LE, Caneda C, Plaza CA, Blumenthal PD, Vogel H, Steinberg GK, Edwards MS, Li G, et al. (2016). Purification and Characterization of Progenitor and Mature Human Astrocytes Reveals Transcriptional and Functional Differences with Mouse. Neuron 89, 37–53. [PubMed: 26687838]

Zhou B, Zuo YX, and Jiang RT (2019). Astrocyte morphology: Diversity, plasticity, and role in neurological diseases. CNS neuroscience & therapeutics 25, 665–673. [PubMed: 30929313]

Highlights

- A method called iβARK to attenuate astrocyte G_q GPCR signaling was validated
- iβARK attenuated astrocyte G_q GPCR signaling *ex vivo* and *in vivo*
- iβARK did not affect astrocyte spontaneous calcium signaling or gene expression
- iβARK revealed astrocytic contributions to behavioral adaptation and memory

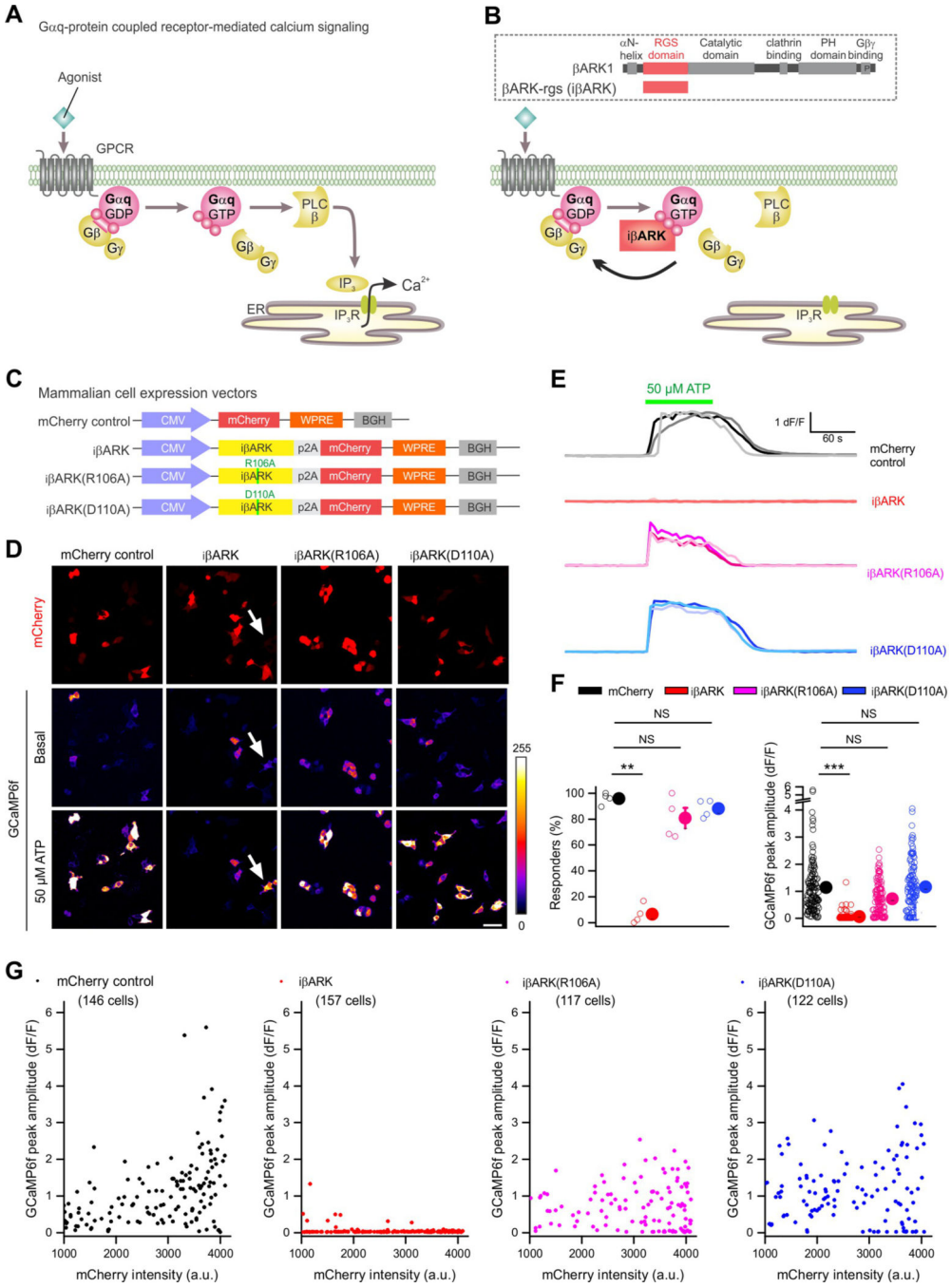

Figure 1. Testing iβARK to attenuate G_q-GPCR-mediated Ca^{2+} signals.

A, Schematics of the $G_{q/11}$ GPCR signaling cascade. When an agonist activates the GPCR, it induces a conformational change that allows the receptor to function as a guanine nucleotide exchange factor (GEF) that exchanges GDP for GTP that is bound to the $G\alpha_q$ subunit, triggering the dissociation of the $G\alpha_q$-GTP subunit from the $G\beta\gamma$ dimer. $G\alpha_q$-GTP stimulates the membrane-bound phospholipase Cβ (PLC), which then cleaves phosphatidylinositol 4,5-bisphosphate (PIP_2) into two second messengers, diacyl glycerol (DAG) and inositol 1,4,5-trisphosphate (IP_3), leading to the activation of IP_3 receptor on the

membrane of endoplasmic reticulum (ER) and the release of Ca^{2+} from ER to intracellular space. **B,** Illustration of the blockade of G_q-GPCR pathway signaling cascades by the iβARK-rgs. Schematic in dotted box illustrates the organization of β adrenergic receptor kinase 1 (βARK1) and βARK-rgs, a peptide containing RGS domain of iβARK1. Bottom, iβARK-rgs directly binds to $G\alpha_q$/11 subunits and thus sequesters them to block subsequent G_q-GPCR-induced signaling cascades (iβARK). **C,** Schematic of the HEK-293 cell vector constructs. **D,** Images of HEK-293 cells expressing mCherry with iβARK, iβARK(R106A) or iβARK(D110A). GCaMP6f was co-expressed to report intracellular Ca^{2+} before and during ATP (50 μM) bath application. ATP induced intracellular Ca^{2+} elevations in absence of iβARK (mCherry control), but not in iβARK-expressing cells. Notably, a cell without mCherry expression (arrow, indicating no expression of iβARK) responded to ATP. In the presence of non-binder controls iβARK(R106A) and iβARK(D110A), intracellular Ca^{2+} was increased by ATP stimulation. **E,** Representative traces for ATP responses in HEK-293 cells expressing control, iβARK, iβARK(R106A) or iβARK(D110A). **F,** The left scatter graph shows the average percentage of responders (%) to ATP. n = 4 transfections for each experimental configurations. One-way ANOVA test was used. The right scatter graph shows the peak amplitude (dF/F) of ATP response. Data shown as mean ± SEM. n = 4 transfections. Nested one-way ANOVA test was used. n = 117–157 cells from 4 transfections for each experimental configurations. Data shown as mean ± SEM. **G,** Scatterplots showing the relationship between peak amplitude of ATP response (dF/F) and mCherry fluorescence intensity. Full details of numbers, precise *P* values, and statistical tests are reported in Excel file S1. Scale bars, 20 μm in **B**. $*P < 0.05$, $**P < 0.01$. NS, not significantly different.

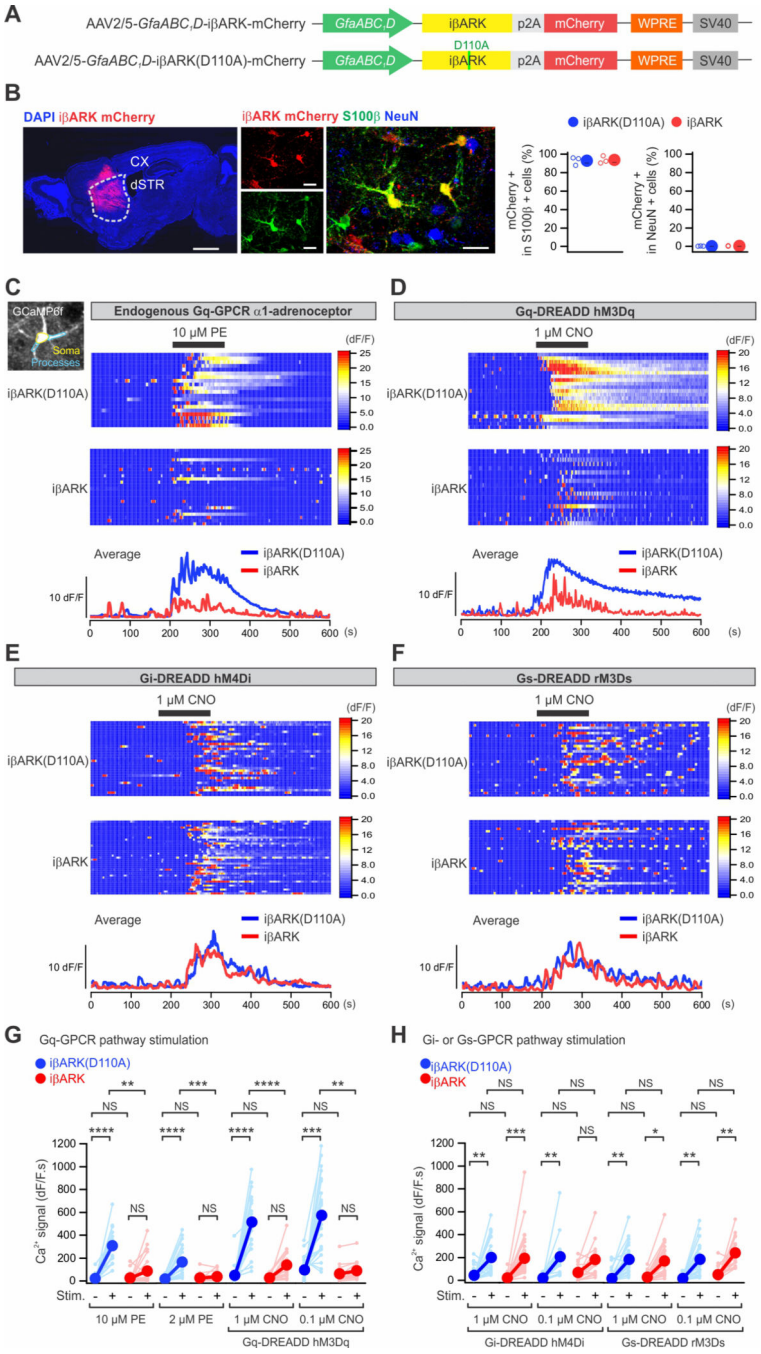

Figure 2. iβARK attenuates G_q-GPCR-induced Ca^{2+} signaling.

(**A**) Schematic of the AAV2/5 constructs for selectively expressing iβARK or iβARK(D110A) in astrocytes. (**B**) The images show that intrastriatal AAV2/5-*GfaABC$_1$D*-iβARK mCherry microinjection resulted in iβARK expression in dSTR (left) with selectivity for astrocytes (right). S100β is a marker for astrocytes (green) and NeuN is a marker for neurons (blue). The scatter graph shows that ~93–94% of the S100β positive astrocytes were iβARK or iβARK(D110A) positive. Little expression in NeuN positive cells (~0.2–0.4%). n = 3 mice. Scale bars, 1 mm (**B,** left) and 20 μm (**B,** right). (**C-F**)

Maximum intensity projection images and soma (yellow) and processes (light blue) are demarcated (**C**). Kymographs and dF/F traces of Ca^{2+} responses in iβARK(D110A)- and iβARK-expressing dSTR astrocytes evoked by phenylephrine (PE; 10 μM), an agoinst of G_q-coupled α1-adrenergic receptor, or clozapine *N*-oxide (CNO; 1 μM), an synthetic agonist of virally delivered G_q, G_i or G_s-DREADDs selectively expressed in dSTR astrocytes. TTX at 300 nM was applied in bath throughout the experiments. (**G,H**) Summary plots for experiments related to **C-F**. PE- and G_q-DREADD-evoked responses were significantly reduced in dSTR astrocytes by iβARK (**G**), while G_i-DREADD and G_s-DREADD-evoked responses were not (**H**). Nested one-way ANOVA test was used. Full details of numbers, precise *P* values, and statistical tests are reported in Data S1. Average data are shown as mean ± SEM. In some cases, the SEM symbol is smaller than the symbol for the mean. $*P < 0.05$, $**P < 0.01$, $***P < 0.001$, $****P < 0.0001$. NS, not significantly different.

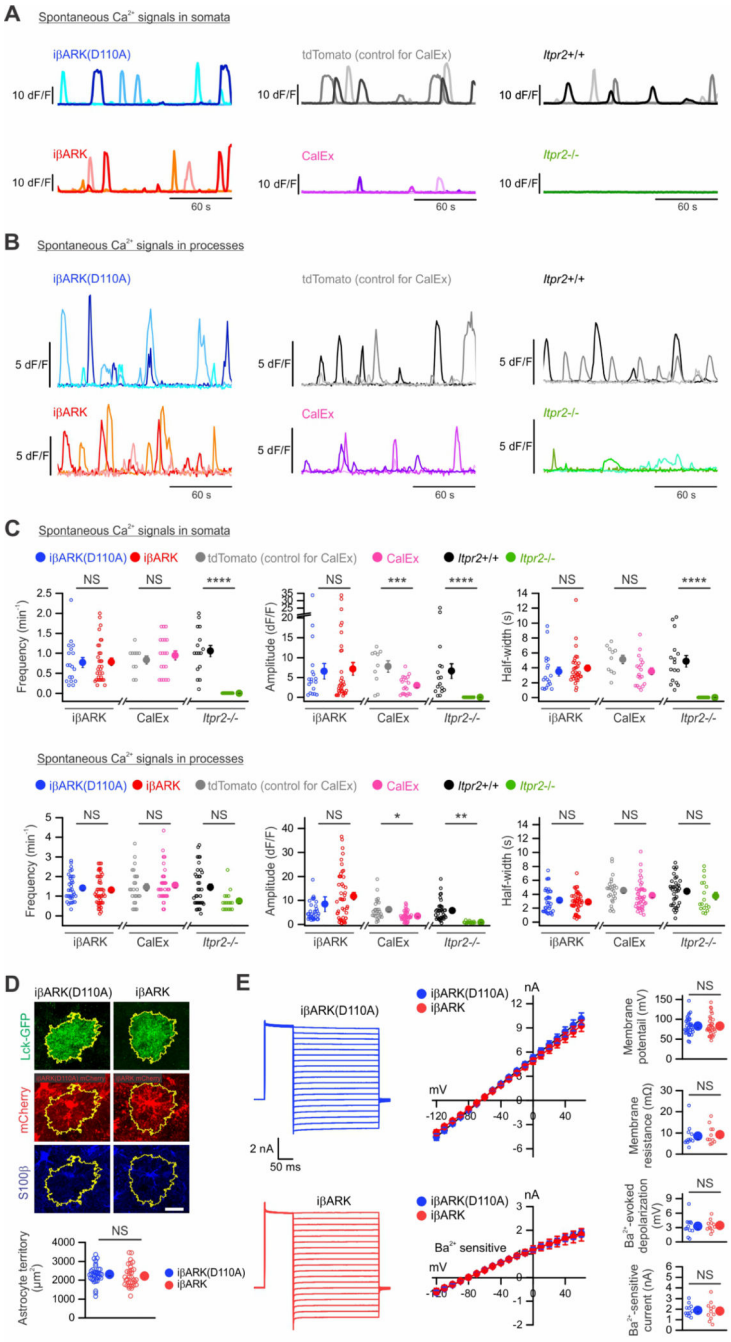

Figure 3. iβARK did not affect spontaneous Ca^{2+} signals, morphology or electrophysiological properties of astrocytes.

(**A**) dF/F traces for somatic spontaneous Ca^{2+} signals from dSTR astrocytes with virally expressed iβARK(D110A) or iβARK, tdTomato (AAV infection control for CalEx) or CalEx, or from wild-type (*Itpr2*$^{+/+}$) or IP_3R2 deletion (*Itpr2*$^{-/-}$) mice. Three representative traces from 3 astrocytes are shown for each condition. (**B**) As in A, but for astrocyte processes. (**C**) The frequency, dF/F amplitude, and half-width of spontaneous Ca^{2+} events were not significantly altered by iβARK. CalEx significantly reduced the amplitude and

half-width of spontaneous Ca^{2+} events, while no alteration was observed in frequency. No spontaneous Ca^{2+} event was detected in astrocyte somata from *Itpr2*$^{-/-}$ mice. N = 3–6 mice in each experiment. Nested t test was used. (**D**) Immunohistochemical analysis of a sparsely labelled dSTR astrocyte expressing Lck-GFP along with iβARK or iβARK(D110A). No change in astrocyte territory area was found between groups. n = 33–36 astrocytes from 3 mice per group. Mann–Whitney U test was used. (**E**) Traces and averaged data for astrocyte current-voltage relationships (−120 to +60 mV) from iβARK or iβARK(D110A) expressing dSTR astrocytes. n = 11–12 astrocytes from 4 mice per group. Mann–Whitney U test was used. Scale bar: 20 μm in **D**. Full details of numbers, precise *P* values, and statistical tests are reported in Excel file S1. Average data are shown as mean ± SEM. In some cases, the SEM symbol is smaller than the symbol for the mean. **P* < 0.05, ***P* < 0.01, ****P* < 0.001, *****P* < 0.0001. NS, not significantly different.

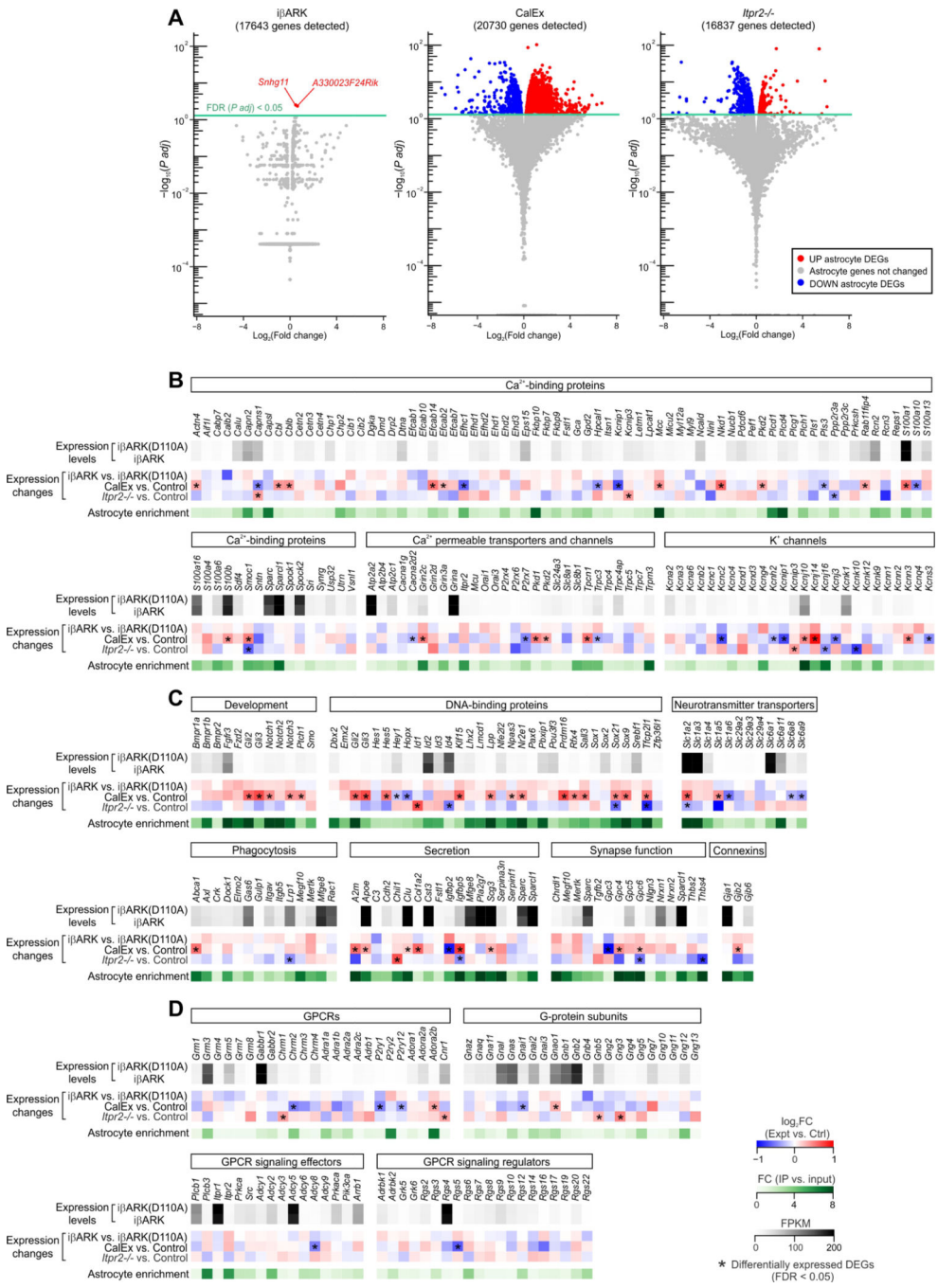

Figure 4. Limited gene expression changes in iβARK astrocytes.

(**A**) Volcano plots showing gene expression changes and corresponding significance in iβARK, CalEx and *Itpr2*$^{-/-}$ dSTR astrocytes detected by RNA-seq relative to their controls. Each dot represents a gene. In all panels, the red dots represent significantly upregulated genes while the blue dots represent significantly downregulated genes. Significance was determined by adjusted *P* values (FDR; false discovery ratio) of < 0.05. n = 4 mice. (**B-D**) List of genes that encode Ca^{2+}-binding proteins, Ca^{2+} permeable transporters and channels, K^+ channels (**B**), proteins involved in development, DNA binding,

neurotransmitter transport, phagocytosis, secretion, synapse function and gap junctions (**C**), GPCRs, G-protein subunits, GPCR effectors and regulators (**D**). Gene expression levels in iβARK(D110A) and iβARK astrocytes were shown as FPKM values. Expression changes were indicated by $\log_2$(Fold change) in iβARK-expressing, CalEx-expressing and *Itpr2*$^{-/-}$ astrocytes relative to their controls. Astrocyte enrichment was plotted as fold change of expression between IP and input samples. Genes with FPKM > 1 were selected for **B-D**. * indicates the genes that were differentially expressed with FDR < 0.05.

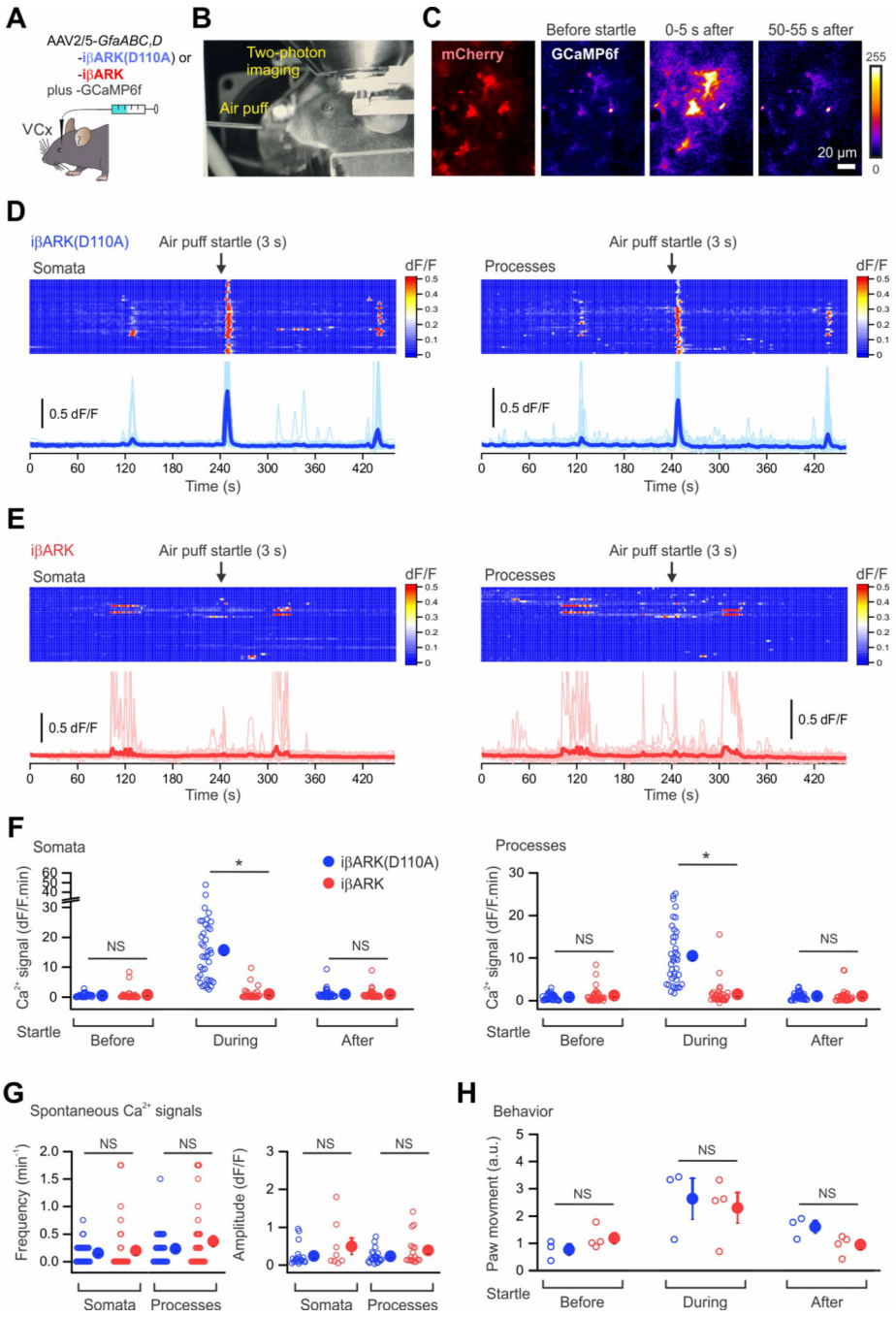

Figure 5. Reduced startle-evoked astrocyte Ca^{2+} signaling by iβARK.

(A) Illustration showing the astrocyte-selective AAV2/5 reagents and approaches for expressing iβARK(D110A) or iβARK in the visual cortex (VCx). (**B**) A representative image showing the *in vivo* 2PLSM setup for head-fixed, awake mice in an acrylic tube. An air pump outside the microscope enclosure was used to generate an unexpected air puff, which evoked startle response. (**C**) Representative pseudo-colored images showing the fluorescence increase of GCaMP6f in astrocytes of mouse visual cortex before, during, and after startle. (**D-E**) Kymographs and dF/F traces of Ca^{2+} responses in iβARK(D110A)-

and iβARK-expressing astrocytes evoked by startle for somata (**D**) and processes (**E**). Scatter graphs on the right show the individual and average Ca^{2+} responses during startle, indicating that iβARK significantly reduced the responses. n = 38 astrocytes from 3 mice for iβARK(D110A) mice and 34 astrocytes from 4 mice for iβARK mice. (**F**) The frequency and dF/F amplitude of spontaneous Ca^{2+} events in *in vivo* astrocytes of visual cortex were not significantly altered by iβARK. (**G**) The graphs show the spontaneous and startle-evoked movements of iβARKD110 mice (3 mice) and iβARK mice (4 mice) were not significantly different. (**H**) Paw movements of the mice before, during and after air-puff startle. Nested t test was used in **F-H**. Scale bar: 20 μm in **C**. Data are mean ± SEM. In some cases, the error bars are smaller than the symbol used to represent the mean. Full details of numbers, precise *P* values, and statistical tests are reported in Excel file S1. **P* < 0.05. NS, not significantly different.

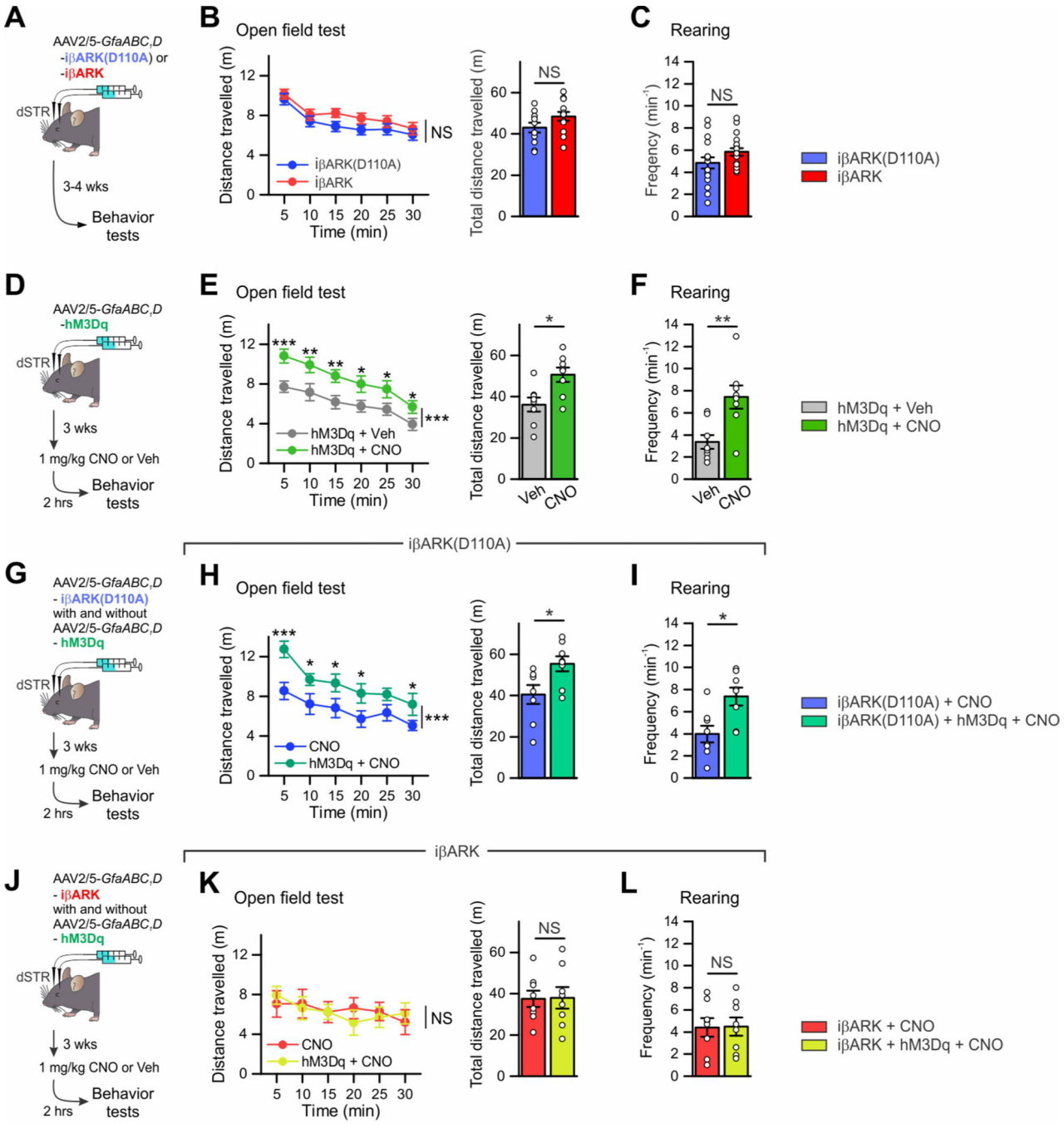

Figure 6. iβARK blocked behavioral hyperactivity induced by G_q-DREADD stimulation in dSTR astrocytes.

(A) Cartoon illustrating the AAV2/5 reagents and approaches for selectively expressing iβARK(D110A) or iβARK bilaterally in dSTR astrocytes. When such mice were prepared, behavior was assessed 3–4 weeks later. (**B**) Distance travelled by the mice over 30 min in an open field chamber, divided into 5 min epochs and also pooled over 30 min for the iβARK(D110A) (11 mice) and iβARK groups (13 mice). (**C**) Rearing frequency over 10 min in the iβARK(D110A) (17 mice) and iβARK groups (18 mice). (**D**) Cartoon

illustrating the AAV2/5 reagents and approaches for selectively expressing G_q-DREADD $hM3D_q$ bilaterally in dSTR astrocytes. Mouse behavior was assessed 3 weeks later and 2 h after i.p. administration of 1 mg/kg CNO or vehicle. (**E**) Distance travelled by the mice over 30 min in an open field chamber, divided into 5-min epochs and also pooled over 30 min for the 2 experimental groups. Astrocyte G_q pathway activation in the dSTR induced behavioral hyperactivity in the open field. n = 8 mice per group. (**F**) Consistent with this, heightened rearing frequency over 10 min was observed in the $hM3D_q$ + CNO group compared to the $hM3D_q$ + Veh group. n = 8 mice per group. (**G**) Cartoon illustrating the astrocyte-selective AAV2/5 reagents and bilateral striatal microinjections for expressing iβARK(D110A) with and without G_q-DREADD $hM3D_q$. Mouse behavior was assessed 3–4 weeks later and 2 h after i.p. administration of 1 mg/kg CNO. (**H-I**) Consistent with **F-G**, the distance travelled by the mice and rearing frequency were greater in the iβARK(D110A) + $hM3D_q$ + CNO group compared to the iβARK(D110A) + CNO group. n = 8 mice per group. (**J**) Cartoon illustrating the astrocyte-selective AAV2/5 reagents and bilateral striatal microinjections for expressing iβARK with and without G_q-DREADD $hM3D_q$. Mouse behavior was assessed 3–4 weeks later and 2 h after i.p. administration of 1 mg/kg CNO. **(K-L**) Heightened locomotive activity in open field and enhanced rearing frequency induced by striatal astrocyte G_q pathway stimulation were blocked by iβARK. n = 8 mice per group. Mann–Whitney U test was used. Data are mean ± SEM. Full details of numbers, precise *P* values, and statistical tests are reported in Excel file S1. **P* < 0.05, ***P* < 0.01, ****P* < 0.001. NS, not significantly different.

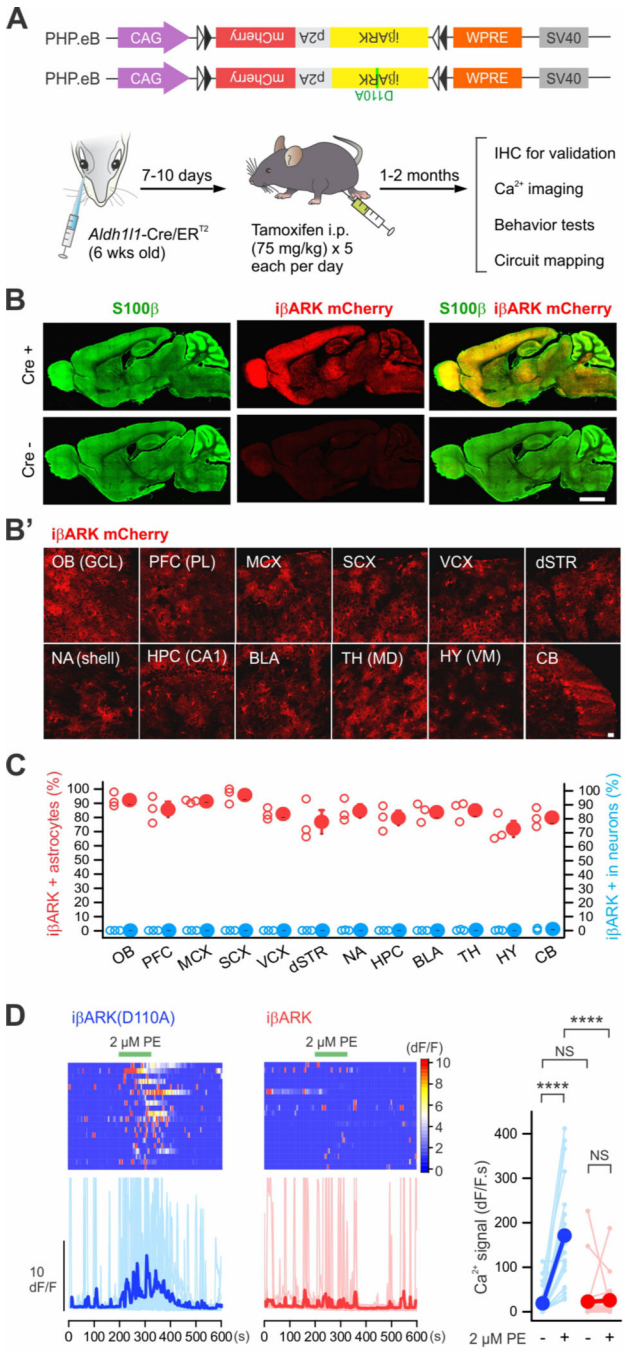

Figure 7. Astrocyte selective iβARK expression in whole brain.

(**A**) Cartoon illustrating the genome constructs packaged by AAV-PHP.eB capsids and an intersectional genetic approach for expressing iβARK or iβARK(D110A) in astrocytes in whole brain by administrating Cre-dependent AAV-PHP.eB viruses into *Aldh1l1*-Cre/ER^{T2} mice. (**B**) Representative images showing that whole brain expression of iβARK was observed in *Aldh1l1*-Cre/ER^{T2}-positive mice, but not in Cre negative mice. AAV-PHP.eB-mediated iβARK delivery resulted in expression within S100β positive astrocytes. Subpanel **B'** shows iβARK mCherry expression in the granule cell layer (GCL) of olfactory bulb

(OB), the prelimbic (PL) subregion of prefrontal cortex (PFC), the layers II/III of the motor cortex (MCX), the sensory cortex (SCX), the visual cortex (VCX), the dorsal striatum (dSTR), the nucleus accumbens shell (NA shell), the hippocampal region CA1 (HPC CA1), the basolateral amygdala (BLA), the mediodorsal thalamus (TH MD), the ventromedial hypothalamus (HY VM) and the cerebellum (CB). (**C**) The red scatters show that 72 – 96% of astrocytes were iβARK mCherry positive in the indicated 12 brain regions. The blue scatters show that those regions had few iβARK mCherry positive neurons (0 – 1%). n = 3 mice. (**D**) Kymographs and dF/F traces of Ca^{2+} responses in dSTR astrocytes with AAV-PHP.eB-mediated iβARK(D110A) or iβARK expression. PE (2 μM) evoked G_q pathway-mediated Ca^{2+} signaling was significantly attenuated by iβARK. Tetrodotoxin (TTX) at 300 nM was applied in bath throughout the experiments. The graph shows summary plots for the Ca^{2+} responses. Nested one-way ANOVA was used. Scale bars, 2 mm in **B** and 20 μm in **B'**. Full details of numbers, precise *P* values, and statistical tests are reported in Excel file S1. Average data are shown as mean ± SEM. In some cases, the SEM symbol is smaller than the symbol for the mean. ****$P < 0.001$. NS, not significantly different.

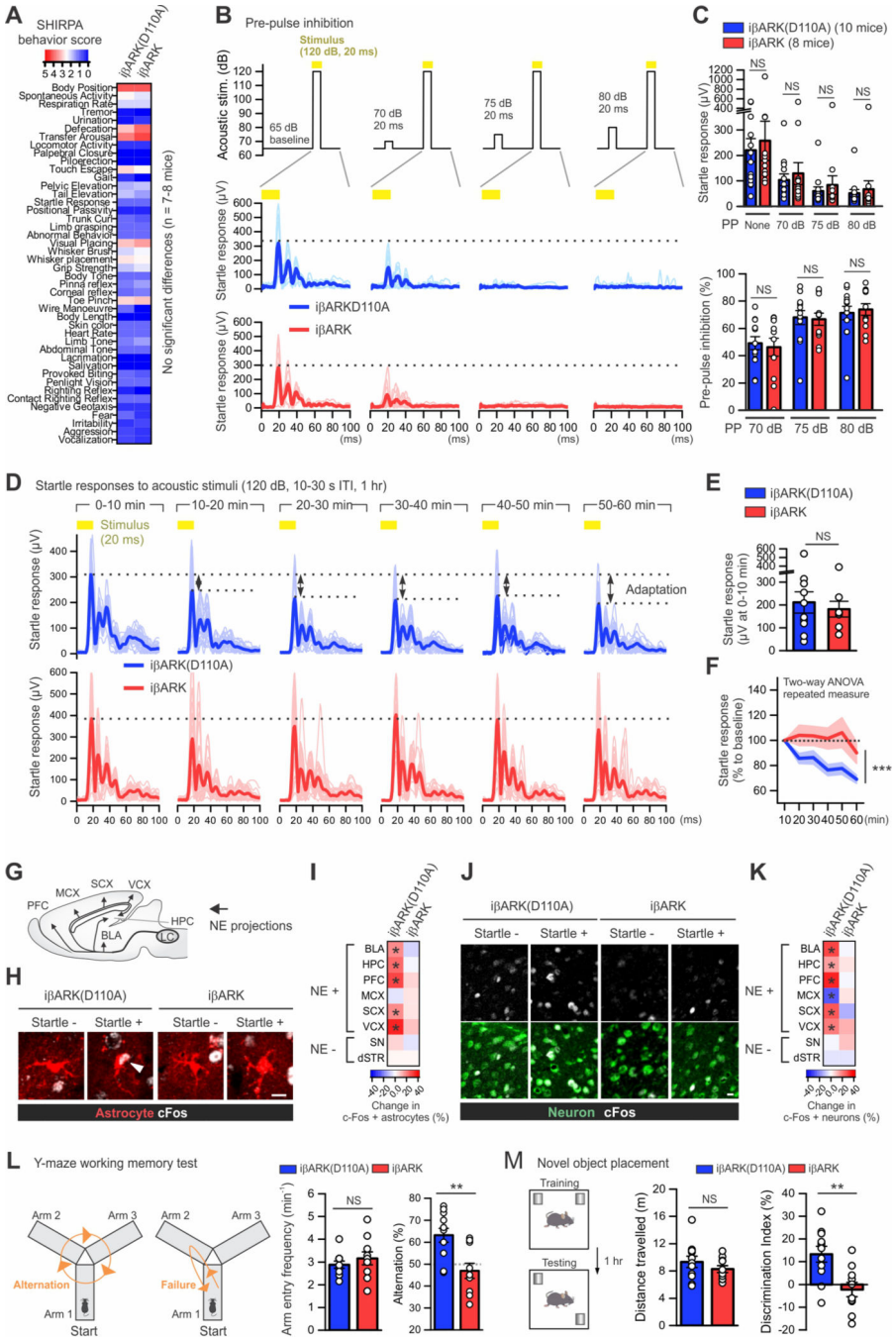

Figure 8. Brain-wide attenuation of astrocyte G_q pathway alters some mouse behavior.

(**A**) Heat map showing the behavioral scores of the SHIRPA battery for phenotype screening. n = 7–8 mice per group. (**B**) Pre-pulse inhibition test. Top, the amplitude and timing of acoustic stimuli with and without pre-pulse (70, 75 or 80 dB, 20 ms) that was initiated 100 ms prior to the stimulus (yellow; 120 dB, 20 ms). Center and bottom, mouse startle responses to the stimuli (yellow) obtained via the accelerometer. Plots in light colors shown individual data from each response, and those in dark colors and thicker lines indicate averaged data. (**C**) Top, summary plot of mouse startle responses to the stimuli with

and without pre-pulses (PP). Bottom, summary plot of pre-pulse inhibition with different amplitude of pre-pulses. Mann–Whitney U test was used. (**D**) Startle adaptation. Mice were exposed to repetitive acoustic stimuli (yellow; 120 dB, 10–30 s inter-trial interval [ITI]) for 1 hour for assessing startle adaptation. The graph plots mouse startle responses in a iβARK(D110A) mouse and a iβARK mouse. Plots in light colors shown individual data from each response, and those in dark colors and thicker lines indicate averaged data over 10 min. (**E-F**) The graphs show the startle responses in iβARK(D110A) mice (10 mice) and iβARK mice (8 mice). (**E**) The startle responses during the first 10 min were not different between the 2 experimental groups. Mann–Whitney U test was used. (**F**) However, the startle response was progressively reduced over 1 hour (i.e. startle adaptation) in the iβARK(D110A) group but not in the iβARK group. Two-way repeated measures ANOVA was used. (**G-I**) Assessment of c-Fos expression in astrocytes in multiple brain areas of the iβARK(D110A) and iβARK groups with and without startle stimuli (n = 4 mice per group). Panel **G** schematize key brain areas receiving norepinephrine (NE) projections. (**H**) Images show astrocytes in the prelimbic prefrontal cortex (PFC) from each group. The arrowhead indicates c-Fos positive astrocytes. (**I**) Heat map on the right summarizes the change in c-Fos positive astrocytes assessed in such experiments. Locus coeruleus, LC; basolateral amygdala, BLA; hippocampus, HPC; prefrontal cortex, PFC; motor cortex, MCX; sensory cortex, SCX; visual cortex, VCX; substantia nigra, SN; dorsal striatum, dSTR. Mann–Whitney U test was used. (**J-K**) Assessment of c-Fos expression in neurons in multiple brain areas in indicated 4 experimental groups. (**J**) Images show that c-Fos in neurons of prelimbic PFC was significantly upregulated in the iβARK(D110A) group but not in the iβARK group. (**K**) Heat map on the right summarizes the change in c-Fos positive neurons assessed in such experiments. Mann–Whitney U test was used. (**L**) Y-maze test for assessing spatial working memory. The cartoons illustrating mice in Y-maze who can freely explore the arms. The left cartoon is an example of successful spontaneous alternation in explorations of arms which requires spatial working memory. The right cartoon illustrates a failed alternation. The left bar graph indicates that the frequency of arm entry was not different between groups. The right bar graph shows that the percentage of alternation in the iβARK group (10 mice) was below chance rate (50%) and significantly lower than in the iβARK (D110A) group (11 mice), indicating impaired working memory. Mann–Whitney U test was used. (**M**) Behavioral layout of the novel object placement task which requires spatial memory. Bar graphs show that the two indicated groups explored the arena similarly (left), however, the iβARK group displayed clear deficits in discrimination of familiar and novel place of objects (right). Mann–Whitney U test was used. Scale bars 10 μm in **J** and 20 μm in **L**. $*P < 0.05$. Full details of numbers, precise P values, and statistical tests are reported in Excel file S1. Average data are shown as mean ± SEM. $**P < 0.01$, $***P < 0.001$. NS, not significantly different.

KEY RESOURCES TABLE

REAGENT or RESOURCE	SOURCE	IDENTIFIER
Antibodies		
mouse anti-S100β	Sigma-Aldrich	Cat# S2532; RRID:AB_477499
rabbit anti-S100β	Abcam	Cat# ab41548; RRID: AB_956280
mouse anti-NeuN (clone A60)	Millipore	Cat# MAB377; RRID: AB_2298772
chicken anti-GFP	Abcam	Cat# ab13970; RRID: AB_300798
rabbit anti-RFP	Rockland	Cat# 600–401-379; RRID: AB_2209751
rabbit anti-c-Fos	Millipore	Cat# ABE457; RRID: AB_2631318
Alexa Fluor 488 goat anti-chicken	Molecular Probes	Cat# A11039; RRID: AB_2534096
Alexa Fluor 488 goat anti-rabbit	Molecular Probes	Cat# A11008; RRID: AB_143165
Alexa Fluor 546 goat anti-mouse	Molecular Probes	Cat# A11003; RRID: AB_2534071
Alexa Fluor 546 goat anti-chicken	Molecular Probes	Cat# A11040; RRID: AB_2534097
Alexa Fluor 594 goat anti-rabbit	Molecular Probes	Cat# R37117; RRID: AB_2556545
Alexa Fluor 647 goat anti-rabbit	Molecular Probes	Cat# A21245; RRID: AB_ 2535812
Bacterial and Virus Strains		
pcDNA 3.1 CMV-iβARK-p2A-mCherry	This paper	Addgene Vectors #117689
pcDNA 3.1 CMV-iβARK(D110A)-p2A-mCherry	This paper	Addgene Vectors #117690
CMV-iβARK(R106A)-p2A-mCherry	This paper	Addgene Vectors #117688
AAV2/5 *GfaABC$_1$D*-iβARK-p2A-mCherry	This paper	Addgene Vectors #117691
AAV2/5 *GfaABC$_1$D*-iβARK(D110A)-p2A-mCherry	This paper	Addgene Vectors #117692
PHP.eB AAV CAG-FLEx-iβARK-p2A-mCherry	This paper	Addgene Vectors #117693
PHP.eB AAV CAG-FLEx-iβARK(D110A)-p2A-mCherry	This paper	Addgene Vectors #117694
AAV2/5 *GfaABC$_1$D* cyto-GCaMP6f	Chai et al., 2017	Addgene Vectors #52925-AAV5 RRID:Addgene_52925
AAV2/5 *GfaABC$_1$D* Rpl22HA	Yu et al., 2018	Addgene Vectors #111811 RRID:Addgene_111811
AAV5 *GfaABC$_1$D*-mCherry-hPMCA2w/b	Yu et al., 2018	Addgene Vectors #111568 RRID:Addgene_111568
AAV2/5 *GfaABC$_1$D* hM3Dq-mCherry	Chai et al., 2017	Addgene Vectors #92284 RRID:Addgene_92284
AAV2/5 *GfaABC$_1$D* hM4Di-mCherry	Chai et al., 2017	Addgene Vectors #92286 RRID:Addgene_92286
AAV2/5 *GfaABC$_1$D* rM3Ds-mCherry	Chai et al., 2017	Addgene Vectors #92285 RRID:Addgene_92285
AAV2/5 *GfaABC$_1$D* Lck-GFP	Shigetomi et al., 2013	Addgene Vectors #105598-AAV5 RRID:Addgene_105598
Chemicals, Peptides, and Recombinant Proteins		
Formalin, Buffered, 10%	Fisher Chemical	Cat# SF100–20
Pronase	Sigma-Aldrich	Cat# P6911
Fetal bovine serum	Thermo Fisher Scientific	Cat# 10437028
BSA	Sigma-Aldrich	Cat# A8806

REAGENT or RESOURCE	SOURCE	IDENTIFIER
Actinomycin D	Sigma-Aldrich	Cat# A1410
TTX	Cayman Chemical	Cat# 14964
R-baclofen	Tocris	Cat#0796
Clozapine N-oxide (CNO)	Tocris	Cat#4936
ATP	Tocirs	Cat#3245
Adenosine	Tocirs	Cat#3624
Phenylephrine	Tocris	Cat#2838
Tamoxifen	Sigma-Aldrich	Cat#T5648
Experimental Models: Organisms/Strains		
Mouse: *Itpr2*$^{tm1.1Chen}$	Li et al., 2005 (gift from Martin Paukert at UT San Antonio)	RRID:MGI:3641042
Mouse: B6;FVB-Tg(Aldh1l1-cre/ERT2)1Khakh/J	Srinivasan et al., 2016	RRID:MGI:5806568
Mouse: C57Bl/6NJ	Jackson Laboratory	RRID: IMSR_JAX:005304
Software and Algorithms		
OriginPro 2016	Origin Lab Corporation	RRID:SCR_015636 https://www.originlab.com/origin
pCLAMP10.4	Molecular Devices	RRID:SCR_011323 https://www.moleculardevices.com
ClampFit10.4	Molecular Devices	N/A https://www.moleculardevices.com
Fluoview FV10-ASW	Olympus	N/A https://www.olympus-lifescience.com/
ImageJ v1.51h	NIH	RRID:SCR_003070 https://imagej.nih.gov/ij/download.html
CorelDraw X7	Corel Corporation	RRID:SCR_014235 https://www.coreldraw.com
Labview 2011	National Instruments	RRID:SCR_014325 https://www.ni.com/
Bioconductor	Bioconductor	http://www.bionconductor.org
GraphPad Prism	GraphPad Software LLC	RRID:SCR_002798 https://www.graphpad.com
Deposited Data		
Bulk tissue and astrocyte RNA-seq: iβARK vs iβARK(D110A)	This paper	GEO: GSE158876
Statistical tests and results	Excel File S1	N/A